

## Article

# Investigation of the Impact of Natural Fracture Geomechanics on the Efficiency of Oil Production and CO<sub>2</sub> Injection from/to a Petroleum Structure: A Case Study

Wiesław Szott \*, Piotr Ruciński, Małgorzata Słota-Valim  and Krzysztof Sowizdzał

Oil and Gas Institute-National Research Institute, 25A Lubicz Str., 31-503 Cracow, Poland; rucinski@inig.pl (P.R.); slota-valim@inig.pl (M.S.-V.); sowizdzal@inig.pl (K.S.)

\* Correspondence: szott@inig.pl; Tel.: +48-606-431-704

**Abstract:** The paper addresses the problem of geomechanical effects in the vicinity of production/injection wells and their impacts on the processes of enhanced oil recovery by CO<sub>2</sub> injection and CO<sub>2</sub> sequestration in a partially depleted oil reservoir. In particular, it focuses on natural fracture systems and their dynamics caused by variations in the rock geomechanical state due to reservoir pressure changes during production/injection processes. The comprehensive approach to the problem requires the combined modeling of both geomechanical and flow phenomena associated with effective coupling simulations of their evolution. The paper applies such an approach to a real, partially depleted oil reservoir in Poland. An effective method of coupled geomechanical and dynamic simulations was used together with the natural boundary and initial conditions for both simulation types. In addition, typical operating conditions were applied in analyzing the processes of enhanced oil recovery by CO<sub>2</sub> injection and CO<sub>2</sub> sequestration. The detailed results of relevant modeling and simulations are presented and discussed focusing on various scale consequences, including the reservoir, well, and completion ones. Both general conclusions as well as the ones specific to the analyzed geological structure are drawn; they confirm the significant dependence of well performance on geomechanical effects and point out several key factors for this dependence. The conclusions specific to the analyzed structure concern fracture reactivation in tensile/hybrid failure mode caused by pressure build-up during CO<sub>2</sub> injection and the importance of the fracture-induced aperture changes resulting from the normal stress, while the shear stress is found to be negligible.

**Keywords:** geomechanical effects; transport properties; natural fractures; enhanced oil recovery; CO<sub>2</sub> sequestration



**Citation:** Szott, W.; Ruciński, P.; Słota-Valim, M.; Sowizdzał, K. Investigation of the Impact of Natural Fracture Geomechanics on the Efficiency of Oil Production and CO<sub>2</sub> Injection from/to a Petroleum Structure: A Case Study. *Energies* **2023**, *16*, 4219. <https://doi.org/10.3390/en16104219>

Academic Editor: Pengchun Li

Received: 14 April 2023

Revised: 17 May 2023

Accepted: 18 May 2023

Published: 20 May 2023



**Copyright:** © 2023 by the authors. Licensee MDPI, Basel, Switzerland. This article is an open access article distributed under the terms and conditions of the Creative Commons Attribution (CC BY) license (<https://creativecommons.org/licenses/by/4.0/>).

## 1. Introduction

The injection of CO<sub>2</sub> into subsurface rock formations has been practiced for decades as an enhanced oil (CO<sub>2</sub>-EOR) and gas (CO<sub>2</sub>-EGR) recovery method [1–9]. Another, more recent process inherently involving CO<sub>2</sub> injection into subsurface structures concerns geological CO<sub>2</sub> sequestration [1,7,8,10–15]. Generally, most of those projects were preceded and/or accompanied by process modeling studies. Concise descriptions of such studies follow. W. Al-Masari and coworkers [16] evaluated the potential of a CO<sub>2</sub>-EOR project under the conditions of a specific petroleum reservoir in the Danish sector of the North Sea. A. Ettehadtavakkol, L. W. Lake, and S. L. Bryent [17] performed the field-scale design optimization of coupled CO<sub>2</sub>-EOR and storage operation from the viewpoint of oilfield operations under specific technical and economic assumptions based on the USA circumstances. Y. Gohmian et al. [18] investigated a variety of CO<sub>2</sub> flood design variables related to both EOR and sequestration objectives in sandstone and carbonate reservoirs to maximize profit from oil recovery and maximize the amount of CO<sub>2</sub> stored in the reservoir. R. Sagi, R.K. Agarwal, and S. Banerjee [19] optimized the EOR system to increase the recovery factor with more efficient utilization of injected CO<sub>2</sub>. M. Arnaut and coworkers [20]

performed simulations of 72 reservoir cases followed by economic analyses for different reservoir conditions and injection strategies to examine the feasibility of different scenarios. H. Karimaie and coworkers [21] performed a simulation study carried out on a realistic model of a North Sea oil reservoir to assess the performance of CO<sub>2</sub> flood in oil recovery. They compared various CO<sub>2</sub> injection schemes and found a relatively high utilization ratio of CO<sub>2</sub> floods compared to other EOR techniques. Y. Liu and Z. Rui [22] proposed a so-called storage-driven CO<sub>2</sub> EOR involving the application of dimethyl ether as an additive to CO<sub>2</sub> to improve oil recovery while assisting CO<sub>2</sub> storage in oil reservoirs. Their simulation results showed that the storage-driven CO<sub>2</sub> EOR is superior to conventional CO<sub>2</sub> EOR in expanding a sweeping efficiency and providing a higher CO<sub>2</sub> storage ratio. An analogous solution for improving CO<sub>2</sub> utilization and storage in oil reservoirs was proposed by Y. Liu, Z., and coworkers [23] who demonstrated the advantages of using propanol as another additive to injected CO<sub>2</sub>. X. Zhao, Z. Rui, and X. Liao [24] studied the CO<sub>2</sub> EOR potential and CO<sub>2</sub> storage capacity of three reservoirs characterized by high heterogeneity, high water saturation, and extra-low permeability, and they found promising results that support the effectiveness of CO<sub>2</sub> injection as means of reducing the CO<sub>2</sub> emission to the atmosphere while enhancing oil recovery.

While all the above-cited studies and many more not mentioned here neglected geomechanical aspects of reservoir simulations applied to the EOR processes, T. W. Teklu and coworkers [25] reviewed geomechanical issues related to those processes and showed the geomechanics to play a significant role regarding all phases of CO<sub>2</sub>-EOR and CO<sub>2</sub> sequestration development schemes. Their conclusions were taken into account in several following studies concerning CO<sub>2</sub>-EOR and CO<sub>2</sub> sequestration modeling and simulations. G. Meurer et al. [26] used a geomechanical model of a fractured carbonate reservoir to understand the failure to open a hydraulic fracture and to investigate the effect of pressure depletion and associated stress changes on fault permeability. They concluded a combination of seismic reservoir characterization and geomechanical forward modeling is useful to identify zones of good reservoir quality. Other advantages of geomechanical modeling included investigating the risk of wellbore collapse during underbalanced drilling, explaining the cause of failure to stimulate a well, and understanding the causes and mechanism of early water breakthrough by fault reactivation. H. Jabbari, M. Ostadhassan, and S. Salehi [27] used a coupled code to study the interactions between reservoir flow and geomechanics to model the deformations and stresses in a CO<sub>2</sub>-EOR process for the extremely tight rocks of the Bakken Formation, Williston Basin, USA. That study confirmed positive results of hydraulic fracturing and well stimulation in an effective increase in the oil recovery factor. A. Elyasi, K. Goshtasbi, and H. Hashemolhosseini [28] implemented a partial coupling of a conventional reservoir and geomechanical simulators to study plastic strain development under production and CO<sub>2</sub> injection scenarios for an oil reservoir in the Sarvak Formation, Iran. They found small changes in the permeability and porosity of the reservoir rock due to a rather insensitive stress–permeability relationship for the rock. The geomechanical analysis of the reservoir also showed no sign of plastic strain under the production and gas injection phases. M. J. Rahman, M. Fawad, and N. H. Mondol [29] investigated the hydromechanical effect on geomechanical failure due to injection-induced stress and pore pressure changes in the prospective CO<sub>2</sub> storage site Smeaheia, offshore Norway. They found the pore volume and compressibility significantly influenced the mechanical rock failure and deformation. They also concluded that there was no caprock failure, guaranteeing that the caprock would act as an effective top seal. L. Chiamonte and coworkers [30] developed a geomechanical model of the Teapot Dome oil field in Tensleep Formation, Wyoming, USA, to evaluate the potential for CO<sub>2</sub> injection inducing slip on a fault and threatening seal integrity. They found no risk of the fault reactivating and providing a potential leakage pathway. They also concluded that a precise constraint of the least principal stress is needed to establish a reliable estimate of the maximum reservoir pressure required to fracture the caprock. J. White and coworkers [31] used geomechanical modeling to find the reason for the CO<sub>2</sub> injected into the In Salah storage site migrating

upward into the lower portion of the caprock. They concluded that the simplest and most likely explanation for the observations indicating the leakage is a portion of the lower caprock being hydrofractured but the overall storage complex not being compromised. P. Sharma, S. Ghosh, and A. Tandon [32] studied the behavior of a depleted oil reservoir in the main producing zone of the West Pearl Queen field in the Queen Formation, New Mexico, USA, within the CO<sub>2</sub> EOR project. They presented a comparison of the one-way geomechanically coupled and non-coupled models and concluded the simulation results were significantly influenced by reservoir geomechanical properties. Those results were attributed to the alteration in relative permeabilities caused by changes in geomechanical properties in the coupled model.

An additional and significant concern during the operation of carbon dioxide injection into geological formations is the risk of CO<sub>2</sub> leakage through the overburden [33–38]. To explain and predict this phenomenon as well as many others occurring during production such as subsidence, compaction, casing damage, wellbore stability, and sand production, it is required to incorporate stress changes and rock deformation when pressures and temperatures in a reservoir are changing during the course of production. The physical impact of these aspects of reservoir behavior may be significant and require geomechanical considerations to be taken into account [39].

Currently, conventional reservoir simulators are not able to reproduce the geomechanical impact on the behavior of the reservoir. Instead, separate geomechanical and flow simulations are performed subsequently, and their results are effectively coupled. Various types of coupling were proposed and tested. They include iterative coupling [40], explicit coupling [41], pseudo-coupling [42], and full coupling [43]. Most recently, other methods and techniques were developed employing various numerical approaches, namely the finite element method vs. the finite difference method [44], or addressing specific cases such as hydrofracturing of unconventional reservoirs [45,46] and CO<sub>2</sub> sequestration in aquifers [47]. In particular, the hydromechanical behavior of natural fractures greatly impacts the productivity and injectivity of naturally fractured reservoirs. Therefore, coupled simulations are especially relevant in this type of reservoir due to the strong dependence of the fracture permeability on its aperture. For these cases, the following relationship takes place: the fluid flow affects the geomechanics of the rocks in terms of pore pressure variations occurring during the production and/or injection; the pressure variations affect the effective stress and strain distributions acting on the natural fractures and modifying their opening or closure; this, in turn, affects the fracture permeability and storability, which impact pore pressure behavior, closing the hydromechanical coupled loop. The subject of geomechanical effects in fractured reservoirs is addressed in several papers. The most numerous group of the papers refers to unconventional reservoirs in the aspect of their hydrofracturing or refracturing [48–52]. Another group of papers is focused on CO<sub>2</sub> sequestration cases in aquifers [53,54]. They studied the geomechanical change in storage formation to evaluate the stability of injected CO<sub>2</sub> and to determine induced stress conditions that can result in irreversible mechanical displacement, reactivating natural fractures, or creating additional fractures. Papers of special interest are those covering the subject of geomechanical effects in the functioning of naturally fractured reservoirs. A. Restrepo and coworkers [55] studied a problem of different completion schemes in a stress-sensitive, naturally fractured gas condensate reservoir in the Mirador Formation, Colombian Eastern Cordillera. They performed explicitly coupled geomechanical and flow simulations on conventional, compositional flow models and extended geomechanical models. Assuming a single producing well with various completion schemes (vertical, hydraulically fractured, and multilateral) and a single gas injecting well, they concluded that not accounting for the geomechanical effects would imply an overestimation in the gas and condensate production. It should be noted that the model employed in the study was not calibrated and the authors used an arbitrary relation between permeability changes and effective stress. It is not clear what the dynamics of the natural fractures are concerning the injecting well creating maximum local reservoir pressure. A. Onaisi and coworkers [56]

studied stress-sensitive reservoirs using iterative, two-way coupling between geomechanical and flow simulations. They included a large North Sea chalk reservoir to be evaluated in predicting compaction drive and subsidence, a limestone reservoir from the Middle East to be evaluated for thermal and pressure gradient effects, and a high-pressure field situated in the UK sector of the North Sea for in-fill drilling problems to be solved. In all three cases, the authors drew rather qualitative conclusions for reservoir operators to take into account in the future reservoir functioning and did not present the significance of the geomechanical effects. F. Bourgeois and N. Koutsabeloulis [57] performed a full-field study of a reservoir in the North Sea using the geomechanical and flow simulators on the reservoir models to assess the integrity of the reservoir development plan. They seemed to use a one-way coupling approach and did not provide the reader with the way of permeability updating caused by geomechanical state modifications. The authors did not present any simulation results, and their conclusions are qualitative.

In this paper, we apply an explicit and complete procedure to construct geological, geomechanical, and dynamical models of a real partially depleted, naturally fractured oil and gas reservoir in the Zechstein dolomite formation. The final models are calibrated based on the data from the complete history of production including bottom-hole pressures and gas–oil ratios. The geomechanical effects are included by the effective, two-way coupling of an implicit type obtained from local correlations between transport property modifications and reservoir pressure changes via the geomechanical state. The results of the coupled simulations covering both production and CO<sub>2</sub> injection phases are analyzed at various levels of complexity (reservoir, well, completion).

Simulation studies performed to cover reservoir fluids dynamics, geomechanical state changes, as well as their effective coupling method, were carried out with the employment of the industry-standard, commercial software package by Schlumberger. In particular, geological modeling was performed with Petrel, geomechanical simulations were performed with Visage, and reservoir flow simulations were performed with Eclipse.

### *Geological Setting*

The study area is located on Gorzow Block, Poland, within the main dolomite basin, belonging to the Stassfurt cyclothem, which is the second out of four depositional cycles of evaporitic rocks in Zechstein and constitutes a part of the more extensive south Permian epicontinental basin [58]. The main dolomite sediments are both the source and reservoir rocks, isolated with the thick sequence of sealing evaporitic rocks, including alternating layers of anhydrite, salt rocks, and thin interbeds of shale. The main dolomite sediments and sealing from the base and top evaporitic rocks make up a closed petroleum system [59]. The biggest accumulations of hydrocarbons in the main dolomite reservoir were discovered on Gorzow Block [60], the tectonic unit neighboring the Foresudetic monocline in the south, Szczecin Through in the north, and Midpolish Through in the NE. Gorzow Block in its NW part is related to Midpolish Through—a regional elongated tectonic unit with an uplifted Permian–Mesozoic complex [61]. It consists of isolated blocks accompanied by extensive volcanic covers and a series of clastic deposits in depressions of the Lower Rotliegend age [62]. These erosional relics had a significant impact on the structural development of the overlying Zechstein–Mesozoic sediment complex. During the sedimentation in early Zechstein, thick platforms of anhydrite with a thickness reaching up to 300 m formed and constituted the base for the main dolomite deposits. The significant variability of the structure of the basement was responsible for the occurrence of the different environments during the sedimentation of the main dolomite. These were the platform, the slope of the platform, and zones of deeper sedimentation [63,64]. Within distinguished facies in the main dolomite, which originated from different sedimentation environments, variation in reservoir quality was observed. The best reservoir properties within the study area were found in the shallow barrier and platform-flat zone [65] and in deeper-situated sediments related to the slope of the platform [64,66]. The reservoir properties were affected by diagenetic processes responsible for the development of secondary porosity [65,66]. The

location of the study area on the map of the distribution of paleoenvironments of main dolomite sedimentation on the tectonic sketch of Poland according to [67] and lithological profile in the zone of interest in the reference borehole, including the main dolomite reservoir rock, are presented in Figure 1.

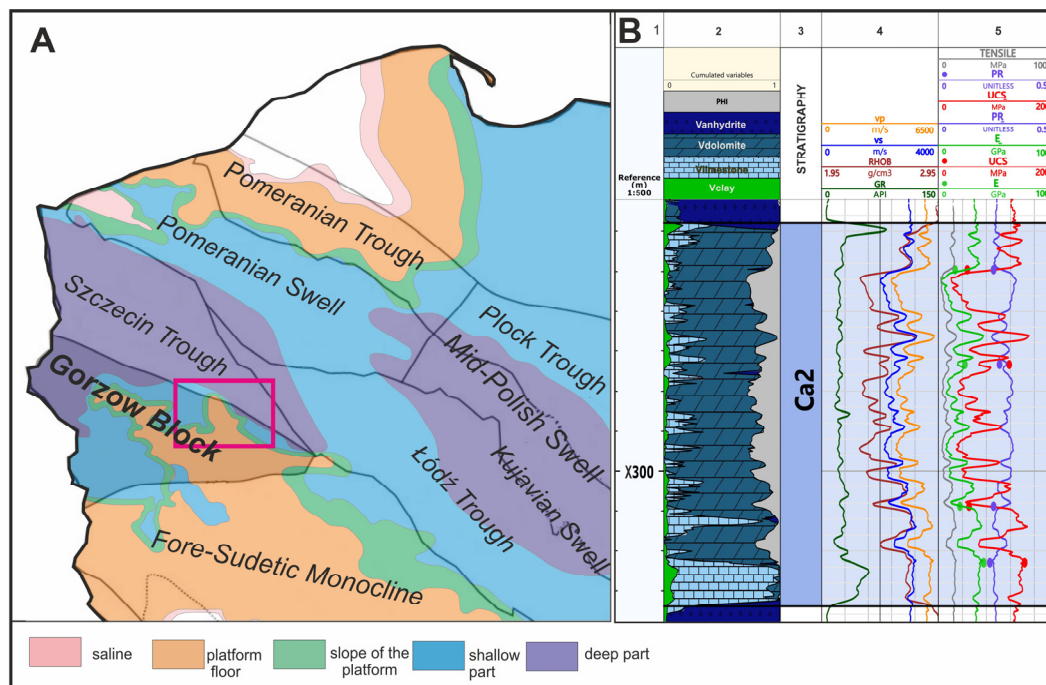


**Figure 1.** Location of the study area marked with a red polygon on the map of the distribution of the paleoenvironments of main dolomite sedimentation on the tectonic sketch of Poland [67] (A). Lithological profile in the reference borehole in the zone of interest with geophysical borehole logging input data; GR—gamma ray, RHOB—rock density,  $v_p$ —compressional wave velocity,  $v_s$ —shear wave velocity (track 4); developed geomechanical logs of Young modulus (E), Poisson's ratio (PR) unconfined compressive strength (UCS), and tensile strength (TENSILE) in the main dolomite reservoir (Ca2) (track 5) (B).

## 2. Geomechanical Effects on EOR Performance

Taking into account geomechanical effects on the performance of enhanced oil recovery (EOR) processes as well as CO<sub>2</sub> storage requires the application of geomechanical modeling coupled with fluid flow modeling to comprehensively evaluate the effectiveness of the EOR process as well as storage characteristics and safety of the geological sequestration in fractured carbonate reservoirs. The change in reservoir formation pressure due to hydrocarbon production and CO<sub>2</sub> injection during CO<sub>2</sub>-EOR and its geological sequestration results in stress field alteration, affecting existing fracture transport properties. A significant increase in pressure can also lead to further fracture propagation, causing the risk of CO<sub>2</sub> leakage through the reservoir overburden. To assess the CO<sub>2</sub>-EOR as well as CO<sub>2</sub> sequestration performance in the fractured reservoir and determine the influence of the fracture on the transport properties, storage capacity, and tightness of the carbonate reservoir, we used numerical methods integrating geomechanical and reservoir fluid flow modeling. A detailed description of the method used in this study to effectively perform coupled simulations of geomechanical and reservoir fluid flow effects is presented in Section 6.

## 3. Geological Modeling

### 3.1. Structural Modeling

The developed 3D structural model of the reservoir zone, its overlying strata, and its embedding (Figure 2B) was used as a basis for the geomechanical and reservoir fluid flow

simulations. The structure of the main dolomite reservoir rock was determined based on the seismic interpretation results, which were constrained with the borehole stratigraphical markers (Figure 2A). The overlying strata included the series of the Zechstein evaporite sequence as follows: basal anhydrite (A2), screening anhydrite (A2G of Stassfurt cyclothem), grey pelite (I3), main anhydrite (A3), younger halite (Na3), top anhydrite (A3G) of Leine cyclothem followed by the lower pegmatite anhydrite (A4D), the youngest halite (Na4), top anhydrite (A4G), and transitional clays (I4) of the Aller cyclothem.

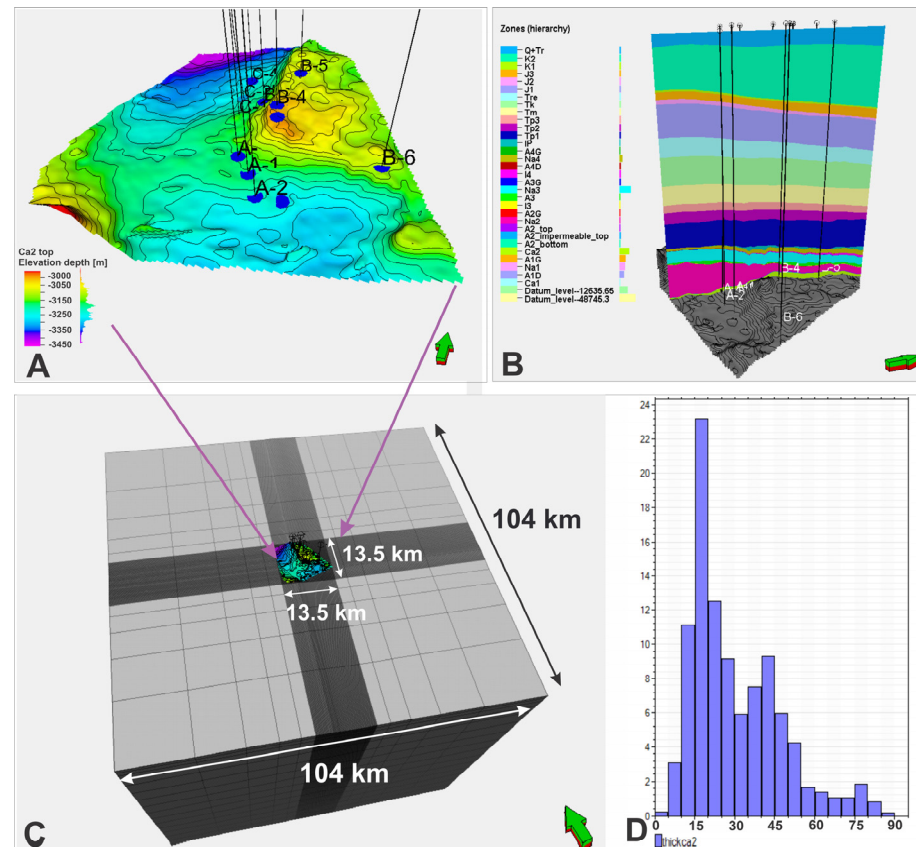


**Figure 2.** The structure of the main dolomite reservoir top with well locations (A); model division into considered zones (B); geometry of the basic model embedded with neighboring rocks for geomechanical simulations (C); distribution of reservoir thickness presented on the histogram (D).

The static geological model of the main dolomite Ca2 with grid horizontal resolution of  $100 \times 100$  m and average vertical resolution of 9.20 m; minimum, maximum, and average reservoir thickness of approx. 0, 90, and 30 m, respectively; and a lateral extent of approx.  $13.5 \times 13.5$  km was embedded with surrounding rocks to apply the boundary conditions properly. The final geometry of the geomechanical embedded model is shown in Figure 2.

### 3.2. Petrophysical Properties

To model petrophysical properties in the main dolomite reservoir rock, we used borehole geophysical logging data and their interpretations performed in the entire borehole profiles, calibrated with the laboratory measurements, and 3D seismic data used as secondary data in the 3D parametric modeling process. To populate the 3D grid extended model to the top surface with density and porosity, we used the well-log data and interpretation results carried out in entire profiles of eight boreholes. The analysis of porosity and density was executed individually for specific lithostratigraphic units and included the determination of variation ranges and semi-variogram modeling of evaluated parameters. For the estimation of 3D porosity and density distributions, a stochastic algorithm was used (Gaussian random function simulation). The calculation of modeled parameter

distributions was repeated 20 times to receive 20 equally probable realizations. The final distribution of density and porosity was an arithmetic average of these realizations, used next in the geomechanical simulation (Figure 3A,B, respectively).

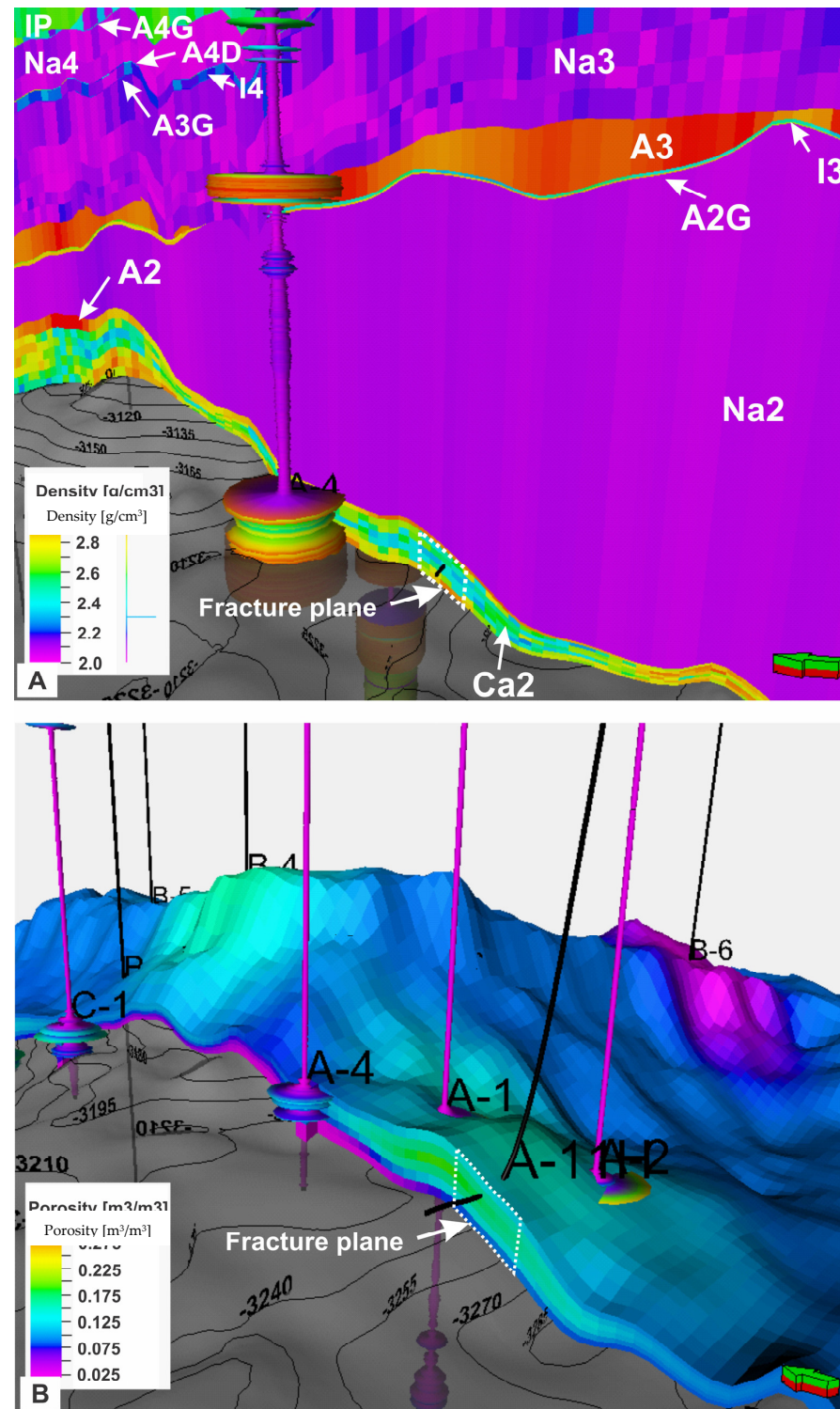


**Figure 3.** Visualization of the 3D density of the reservoir and overlying rocks (A) and porosity model in the Ca2 reservoir rock in the fracture vicinity (B).

The detailed model of petrophysical properties was developed in the Ca2 main dolomite reservoir zone, which was a potential storage formation at the same time. We used well-log

interpretation results calibrated with the dense dataset of laboratory measurements from eight boreholes to model petrophysical properties in the reservoir zone. To enhance model definition, seismic attributes transformed into the seismic properties revealing good correlation with interpreted porosity in the borehole profiles were applied. For calculating porosity distribution, we used the Gaussian random function simulation algorithm with an activated co-kriging option. The obtained porosity distribution is shown in Figure 3. The permeability model was based on the porosity vs. permeability relationship established from the interpretation of permeability in the borehole profiles. Developed models of porosity and permeability determining the pore space volume and the ability of fluids to flow through the reservoir rocks, respectively, provided essential input for reservoir simulations.

#### 4. Geomechanical Modeling

Injection of gas into the reservoir rock as part of the EOR, aiming at increasing the ability of oil flow to enhance the production, followed by long-term injection of CO<sub>2</sub> and its storage involves pressure changes in the reservoir and results in a decrease in the effective stresses [68]. The fractures present in the reservoir can be particularly sensitive to those changes, which can translate to the modification of transport properties and affect the overall performance of enhanced recovery and sequestration processes. In addition, a significant increase in pore pressure may lead to the fracture propagation enhancing permeability of the fracture zone but, on the other hand, posing a threat to the sealing properties of the caprock and potential leakage of CO<sub>2</sub> through the overlying strata.

The initial effective stress conditions in a reservoir and the overlying rocks can be expressed with the following formula dedicated to isotropic rocks [69–71]:

$$\sigma_h - \alpha p = \frac{\nu}{1 - \nu} \times (\sigma_v - \alpha p) + \frac{E}{1 - \nu^2} \times (\epsilon_h + \epsilon_H) \quad (1)$$

To capture the changes in the stress and strain field that can further impact the transport properties, a series of parametric models providing information about the spatial variability of petrophysical and geomechanical properties of the main dolomite reservoir zone and surrounding rocks were developed.

##### 4.1. Modeling of Geomechanical Properties

Three-dimensional geomechanical models of elastic properties such as Young modulus and Poisson's ratio, as well as strength properties including uniaxial compressive (UCS) and tensile strength (T), were constructed using borehole geophysical logging data together with the results of laboratory measurements of static geomechanical properties and 3D seismic data.

The variability in elastic properties along the borehole profile was defined by using sonic well-log data, including the velocity of compressional ( $v_p$ ) and shear waves ( $v_s$ ) and density log utilizing the following relationship [72,73]:

$$v_{dyn} = v_p^2 - v_s^2 / 2 (v_p^2 - v_s^2) \quad (2)$$

$$E_{dyn} = \rho v_s^2 \left[ \left( 3v_p^2 - 4v_s^2 \right) / (v_p^2 - v_s^2) \right] \quad (3)$$

Dynamic elastic properties were then recalculated to the static equivalents using the linear regressions developed in the previous studies dedicated to the main dolomite reservoir rock [74].

For the estimation of the unconfined compressive strength curve, a relationship between compressional wave velocity and UCS of the dolomite rock developed by [74] in the study area was used. Tensile strength along the borehole profile was estimated, taking the reported dependence between UCS and tensile strength, which on average tends to be 10 times smaller than compressive strength [75–77].



#### 4.2. Fracture Properties

The presence of fractures reduces the strength properties of the rock, and the fractured areas become especially sensitive to deformations [83]. Therefore, the fracture zone should be considered and parametrized to fully capture the impact of stress field changes with pressure rise during the application of the EOR method and later on CO<sub>2</sub> sequestration. The presence of the discontinuity zone and its location were deduced, taking into account the drilling report of the A-11H horizontal borehole, indicating a sudden inclination increase in the zone interpreted as a possible 10 m wide discontinuity zone (Figure 5A,C). At the same time, interpreted well logs indicate a permeability rise in this zone (Figure 5C). The implied discontinuity zone was not detected on the 3D seismic image, even though it was processed with the seismic attributes dedicated to fracture and fault detection. In the evaluated case of the main dolomite reservoir (Ca2), the fracture zone was introduced to the geomechanical model as a set of 10 discrete fracture planes with a spacing of 0.5 m and a length of 500 m (Figure 5B).

Estimated initial fracture zone dimensions and geological parameters are depicted in Table 2.

**Table 2.** Fracture zone dimensions and geological initial parameters.

Dimension x, dx (m)	5
Dimension y, dy (m)	500
Dimension z, dz (m)	33–45
Permeability x, kfx (mD)	0.5–450
Permeability y, kfy (mD)	700
Permeability z, kfz (mD)	700
Porosity, $\phi_f$ (%)	0.1

The fracture zone was parametrized using the Petrel Geomechanics materials library. The list of parameters describing the fracture zone can be found in Table 3.

**Table 3.** The discontinuity zone properties assumed in the model (Petrel Reservoir Geomechanics software manual, 2013).

Fracture normal stiffness (bar/m)	22,620
Fracture shear stiffness (bar/m)	9048
Cohesion (bar)	0.01
Friction angle (°)	20
Dilation angle (°)	10
Tensile strength (bar)	0.01
Fracture spacing (m)	0.5
Initial opening (-)	0

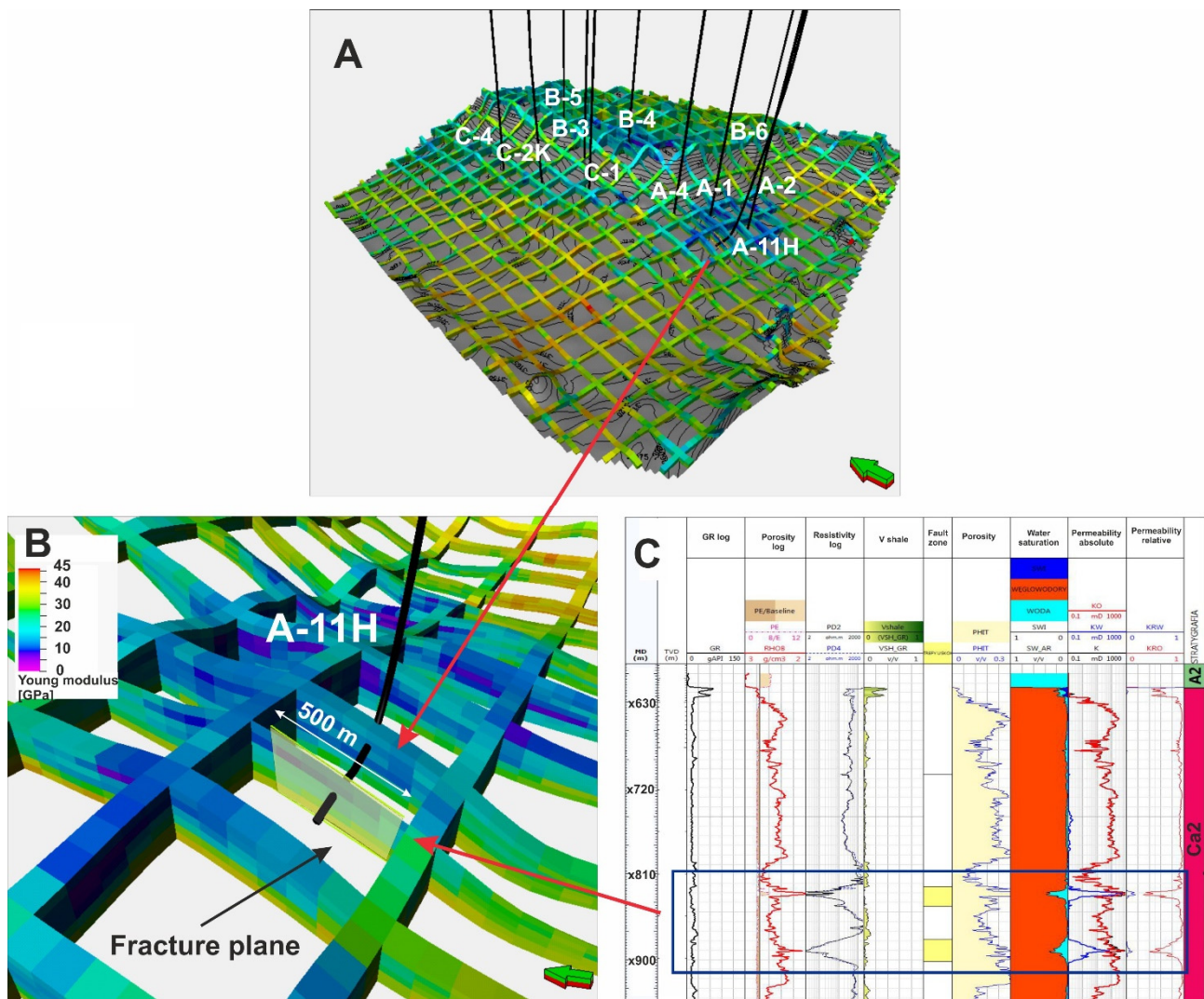


**Figure 5.** Visualization of the fracture zone location on the background of Young modulus distribution in the main dolomite (Ca2) reservoir rock (A) with a focus on the fracture zone (B) with a detected increase in permeability based on the well-log data (C).

#### 4.3. Boundary Conditions

To determine the initial stress conditions, we used the load of the overlying rocks and tectonic stresses as boundary conditions. The direction and magnitude of the maximum horizontal stress were defined using literature data, where the azimuth of the  $\sigma_H$  was defined to be  $6^\circ$  based on the analysis of the breakout failure orientation on the borehole wall while the  $\sigma_h$  gradient was determined to be approx. 0.1707 bar/m based on minifrac tests in the nearest available borehole location [84]. In the reference borehole where the results were available, a normal stress regime was observed. The anisotropy between principal horizontal stresses was also assumed based on the findings from the same reference borehole to be 1.25 [84].

#### 5. Dynamical Modeling

To construct a dynamic model of the analyzed structure, the geological model described in Section 3 was utilized. The dynamical model was supplemented with the following components:

- Initial distributions of reservoir fluids (oil, gas, and water) under the hydrostatically balanced conditions were generated with the J-Leverett function [85] approach so that

- the fluid saturation depth profiles, as determined from geophysical measurements in all the wells, were reproduced;
- Reservoir fluid transport properties (relative permeabilities)—a standard power-like Brooks–Corey model [86],  $k_{rx} = k_{rx,max} (S_{rx})^{n_x}$  ( $x = w,o,g$ ), was adopted for the relative permeability,  $k_{rx}$ , and dependence upon the reduced fluid saturation,  $S_{rx}$ , where  $S_{rx} = \frac{S_x - S_{x,min}}{S_{x,max} - S_{x,min}}$ . The exponent  $n_x$  and endpoint parameters  $k_{rx,max}$ ,  $S_{x,min}$ , and  $S_{x,max}$  were determined in the model calibration procedure, and their values are given in Table 4. Detailed information on the calibration procedure is given in Section 7.
  - A reservoir, hydrocarbon fluid thermodynamical model—a compositional, thermodynamical model of the reservoir hydrocarbon fluid (oil and gas) was constructed and calibrated independently of the reservoir model the history matching procedure, and using the measurement data obtained from the laboratory PVT studies [87], including the pressure of the saturation point, flash tests, differential liberation tests, and separator tests. The model employed the Soave–Redlich–Kwong equation of state and Lorenz–Bray–Clark viscosity model and was characterized by a complete set of EOS parameters for the effective eight-component fluid including both hydrocarbon and non-hydrocarbon ones (Table 5).

**Table 4.** Calibration results of relative permeability curve parameters.

Phase	Parameter	Initial Value	Value after Calibration
water	$n_w$	2	2
water	$S_{w,min}$ ( $=S_{rw}$ )	0.1	0.0528
water	$S_{w,max}$	1	1
oil (oil–water system)	$n_o$	2	2
oil (oil–water system)	$S_{o,min}$	0.4	0.4917
oil (oil–water system)	$S_{o,max}$	1.0	0.9964
oil (oil–gas system)	$n_o$	2	2
oil (oil–gas system)	$S_{o,min}$	$1 - S_{g,max}$	$1 - S_{g,max}$
oil (oil–gas system)	$S_{o,max}$	$1 - S_{g,min}$	$1 - S_{g,min}$
gas	$n_g$	2	2
gas	$S_{g,min}$ ( $=S_{rg}$ )	0.1	0.1
gas	$S_{g,max}$	1	0.9964

**Table 5.** Composition of the reservoir fluid after component grouping.

Component	% mol
N <sub>2</sub>	31.588
CO <sub>2</sub>	0.612
H <sub>2</sub> S	5.085
C <sub>1</sub>	19.353
C <sub>2</sub>	3.567
C <sub>3</sub> –C <sub>6</sub>	11.990
C <sub>7</sub> –C <sub>11</sub>	12.270
C <sub>12</sub> +	15.500

### 6. Two-Way Simulation Coupling

To study the influence of geomechanical effects upon the reservoir fluid flow, effective modeling of fluid flow through porous media and variations in the geomechanical state of these media at different pore pressures and reservoir fluid distributions is required [39,88–91]. In general, precise solutions to this problem require the use of numerical techniques to simultaneously solve coupled equations describing both fluid transport phenomena and geomechanical effects. This approach, called a fully coupled simulation [92–94], is characterized by complex numerical modeling that results in very high computational costs [95]).

An alternative approach uses partially coupled modeling [39,88,96] where an external coupling between separate numerical simulations of both key phenomena is employed. It requires multiple iterative simulations including fluid flow calculations at each time step and stress–displacement calculations at selected time steps only until a full consistency of the solutions is obtained. Another approach was proposed in [97] where local direct dependence between pore pressure variation and basic transport parameter variation via the geomechanical parameter changes is used. The schematic of this procedure is shown in Figure 6 for the time interval  $(t, t + \Delta t)$ .

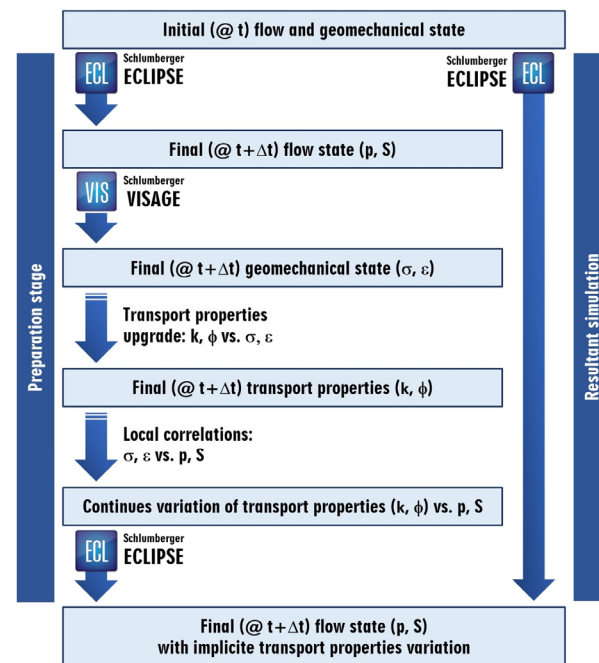


**Figure 6.** The applied procedure of dynamical and geomechanical model coupling.

It is assumed that all basic variables (pore pressure,  $p$ ; fluid saturation,  $S$ ; stress tensor,  $\sigma$ ; strain tensor,  $\varepsilon$ ) describing the process evolve continuously in the time interval  $(t, t + \Delta t)$ . This situation usually takes place when the number of active wells is fixed, their production/injection rates vary smoothly, and there are no failure events in the geomechanical status evolutions. An opposite situation takes place when, e.g., the drilling of new wells causes abrupt changes in the geomechanical status of the reservoir. Consequently, geomechanical simulations are performed at selected time moments coinciding with special events of discontinuous character. By identifying separate regions of a uniform variation in geomechanical state parameters with reservoir pressure changes during continuity intervals, specific correlations can be found for basic parameters (porosity, permeability) as direct functions of pressure in each of the spatial regions and time intervals. At first, correlations between pressure variation and geomechanical state parameters (stress tensor,  $\sigma$ ; strain tensor,  $\varepsilon$ ) are determined from the results of geomechanical simulations. Subsequently, the variation in transport properties (permeability,  $k$ ; porosity,  $\phi$ ) as functions of the geomechanical parameters (e.g., volumetric strain) is applied according to adopted models (e.g., Kozeny–Carman model [98]) in matrix zones. An analogous approach is used to couple geomechanical effects and flow phenomena in fracture zones. Details of this approach are given in the sections below.

### 6.1. Correlation of Geomechanical State and Transport Parameters

For the reservoir matrix correlation between pore pressure changes and volumetric strain, changes were found to be relatively homogeneous. An analogous correlation between reservoir pressure variations and effective stress was established for the fracture zone of the A-11H well (Figure 7A). These results were grouped into six sets corresponding

to six different groups combining two consecutive layers each, and the linear correlations of the groups were parametrized as shown in Figure 7B.

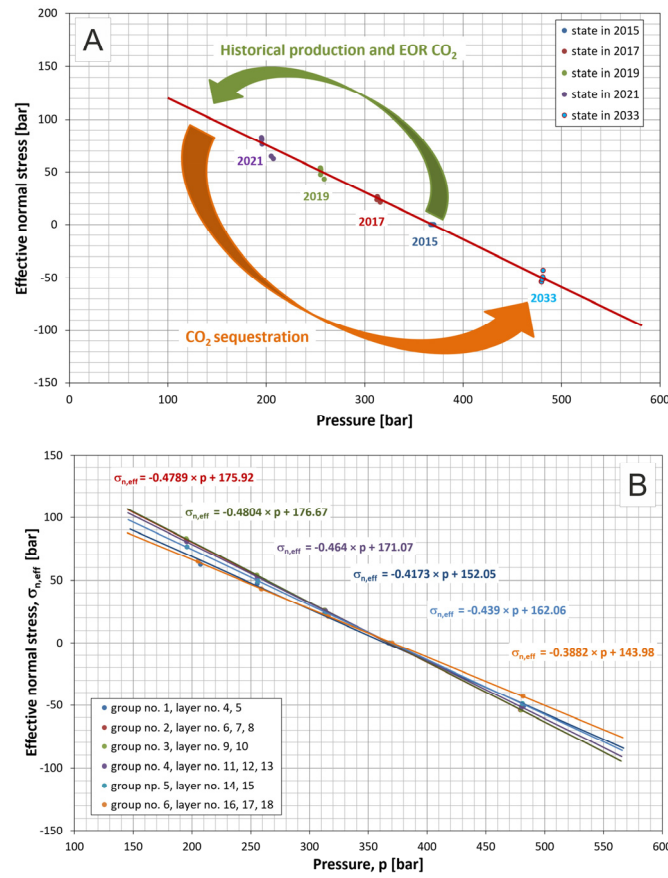


**Figure 7.** Local correlations of effective normal stress changes vs. pore pressure in the fracture zone of A-11H well. (A) Changes for specific time steps. (B) Changes for identified layers in the fracture zone.

### 6.2. Fracture Response to Changes in Geomechanical State

The process of fracture effective permeability variations with changing pressure was applied to the fracture zone of the A-11H well during the history of reservoir operation and the forecast of CO<sub>2</sub> injection into the main dolomite reservoir rock. To this end, a specific model correlating fracture effective apertures and geomechanical states of the fractured rock was adopted following the exponential law studied in [99].

The exponential law effectively describes the nonlinear decline in fracture aperture with increasing effective stress in the fractured rocks [100,101]. In that study, to calculate the equivalent permeability,  $k$ , a normal closure component,  $k_n$ , and a shear dilation component,  $k_s$ , are used in the form of empirical relationships [99] (4)–(6):

$$k = k_n + k_s, \tag{4}$$

$$k_n = \frac{f_n}{12} b^3, \tag{5}$$

$$k_s = \frac{f_d}{12} d^3, \tag{6}$$

The effective aperture,  $b$ , as the function of normal effective stress,  $\sigma_n$ , is given by [99] Equation (7):

$$b = b_r + b_m = b_r + b_{max} \exp(-\alpha' \sigma_n), \tag{7}$$

To calculate effective shear dilation of fractures, the relationship of the exponential dependency of stress ratio,  $\sigma_r$ , and equivalent frictional coefficient,  $q$ , on shear dilation is utilized [99], as shown in Equations (8)–(10) below:

$$d = 0 \text{ for } \sigma_r < q, \quad (8)$$

$$d = d_{max}[1 - \exp\{-\gamma(\sigma_r - q)\}] \text{ for } \sigma_r \geq q, \quad (9)$$

$$\sigma_r = \frac{\sigma_{max}}{\sigma_{min}} \quad (10)$$

To simplify the analysis, we assumed cohesive strength to be negligible. According to Coulomb frictional criterion, the shear strength depends only on the frictional strength and is expressed as the frictional coefficient,  $\mu$ , or equivalent frictional parameter,  $q$ , related to the angle of internal friction,  $\varphi$ , as given by [99] Equation (11):

$$q = \left( \sqrt{\mu^2 + 1} + \mu \right)^2 = \frac{1 + \sin\varphi}{1 - \sin\varphi} \quad (11)$$

The quantity mostly responsible for the permeability decline in the mechanism of the fracture closure is the horizontal stress,  $\sigma_n$ , normal to the fracture plane.

In addition, parameters that determine possible fracture kinematics, namely slip tendency,  $T_s$ , and dilation tendency,  $T_d$ , were calculated. A slip is likely to occur in a fracture plane when the resolved shear stress,  $\tau_s$ , equals or exceeds the frictional resistance to sliding [61]. Therefore, the slip tendency is the ratio of maximum resolved shear stress to normal stress acting in the surface [102]. In the analyzed case, values of the slip tendency ( $0.15 < T_s < 0.25$ ) are too low to meet the condition of the Beyerlee law [103] ( $T_s > 0.6$ ). According to that condition, the fracture is not ideally oriented for the slip in the present stress field. The fracture normal dilation and the fluid transmission ability are directly related to the fracture aperture, which is dependent upon the effective normal stress [102]. The values of dilation tendency ( $0.67 < T_d < 1.00$ ) suggest that fracture reveals a considerable tendency for reactivation relating to extensional movement, increasing through the historical production phase. During the CO<sub>2</sub>-EOR phase, the fracture seems almost ideally oriented for reactivation in tensile or hybrid failure mode. Finally, during the pressure build-up of the CO<sub>2</sub> sequestration period, the fracture tends to reverse back to the tensile failure mode, as shown below in Figure 8.

Nevertheless, after many geomechanical simulations were performed, it was noticed that shear stress-induced dilation is a negligible phenomenon and is not able to effectively affect changes in the fracture aperture with pressure variations. Finally, the calculated stress ratios are much lower than equivalent frictional coefficients ( $\sigma_r \ll q$ ). As a result, the effective normal stress will be the main factor producing changes in the fracture aperture, which, in turn, is responsible for permeability variations. Fractures will tend to reactivate in the hybrid failure mode. After that, they will continue to vary the aperture rather than undergo tractional displacement, for pore pressures under initial reservoir pressure. When CO<sub>2</sub> injection into a formation over initial reservoir pressure but below fracturing pressure is performed, fractures are more likely to experience tensile failure (Figure 9).

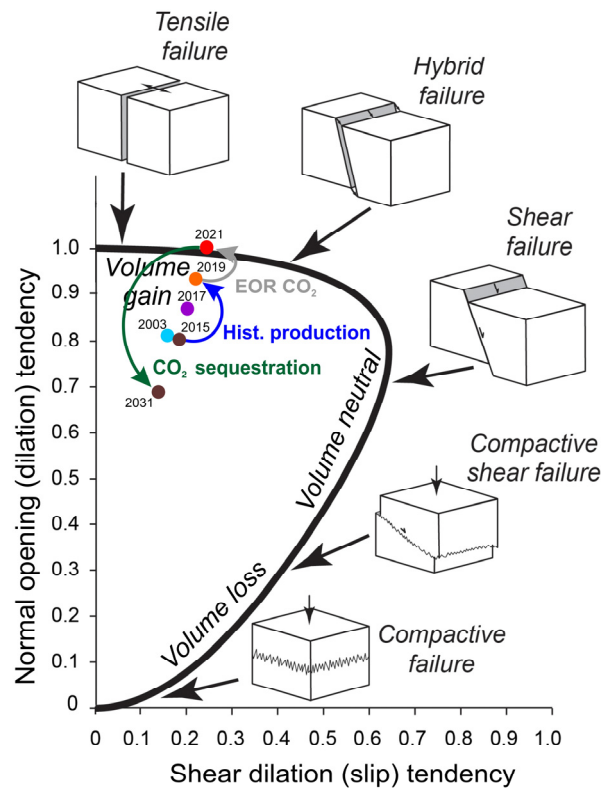


**Figure 8.** Relationship between maximum shear dilation tendency and normal opening tendency with associated rock failures and volume changes (modified after [104]). Evolution of the modeled fracture zone properties.

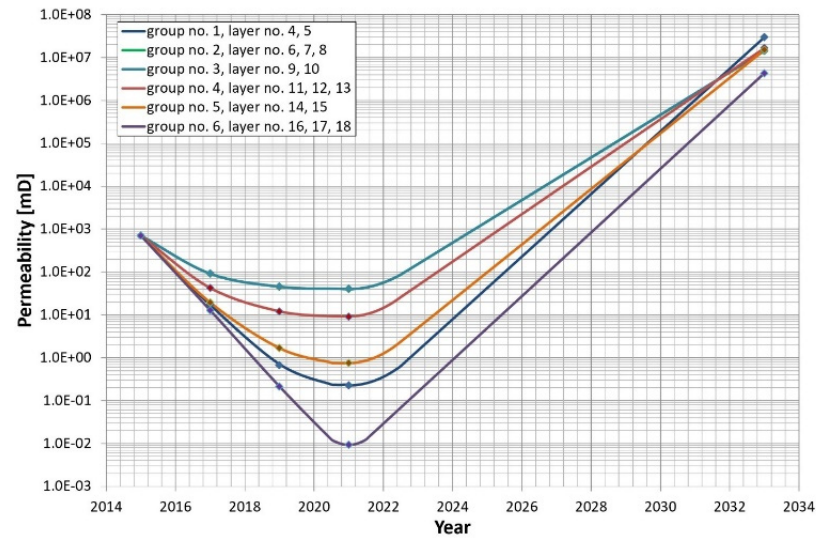


**Figure 9.** Local variations in fracture equivalent permeability vs. time, permeability grouped for reservoir flow model layers, the fracture zone at A-11H well. Note: The curve of group no. 3 is identical with the curve of group no. 2.

The above model of fracture dynamics was applied in the reservoir model calibrations and simulation forecasts as presented in the following sections. An example of explicate evolution of the fracture equivalent permeability is shown in Figure 9.

## 7. Model Calibration

The reservoir simulation model of the analyzed structure was calibrated based on the data obtained from the reservoir operator and covering 16 years of its operation with 11 producing wells. The calibration data consist of daily oil, gas, and water production from individual wells, bottom-hole pressures, and well test results. The calibration procedure was performed in a standard way; i.e., the oil production data were taken as the control data while the other measurements were matched with the modification of both global and local model parameters as listed below.

### 7.1. Calibration Results

The calibration process produced a satisfactory match of the simulation results and the historical operation data. An example of static bottom-hole pressure measurements vs. simulation results in an exemplary A-2K well is shown in Figure 10, and gas–oil ratio measurements vs. simulation results in the same well are shown in Figure 11.

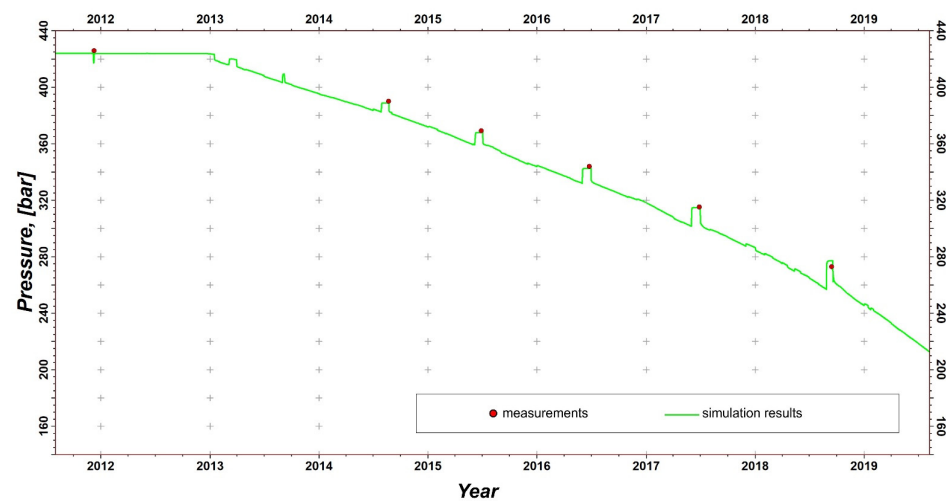


Figure 10. Bottom-hole pressure evolution of A-2K well.

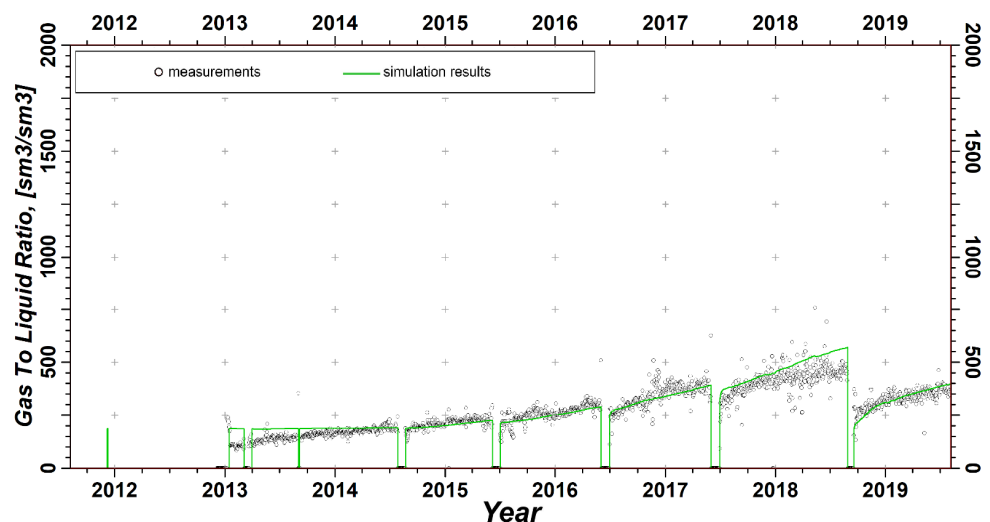
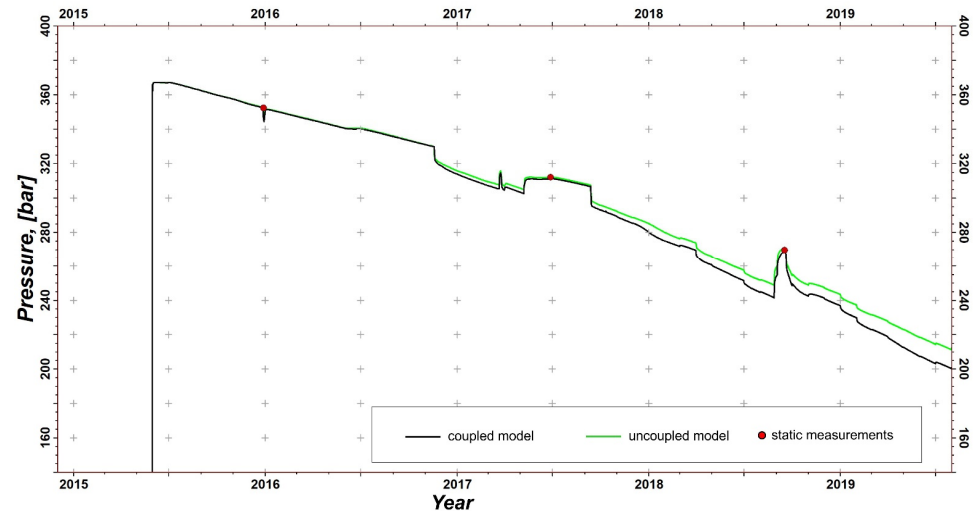


Figure 11. Gas–oil ratio measurements vs. simulation results for A-2K well.

The calibration process resulted in modifications of several model parameters of both global and local types. They included poorly determined quantities such as relative permeabilities, permeability anisotropies, well productivity indices, and skin-effect coefficients. In particular, parameters of the fracture zone identified at the A-11H well were estimated

to produce bottom-hole pressure (BHP) consistent with the measured data as presented in Figure 12 for BHP. In addition, Figure 12 shows a small but distinct difference resulting from the consideration of geomechanical effects on the well performance. Similarly, the results of the gas–oil ratio for the cases taking into account and neglecting geomechanical effects are compared in Figure 13.



**Figure 12.** Bottom-hole pressure measurements vs. simulation results for A-11H well. Impact of the geomechanical effects upon the bottom-hole pressure—coupled vs. uncoupled models.

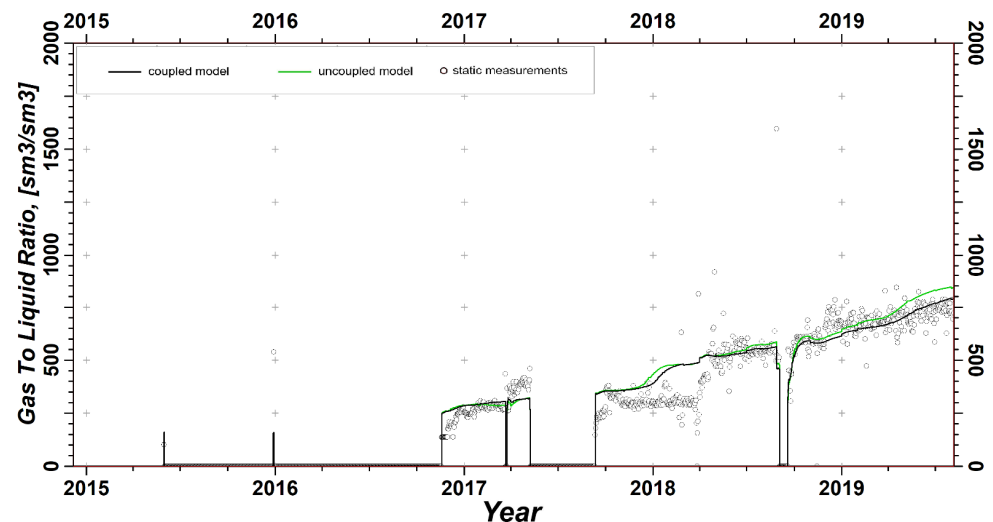


**Figure 13.** Gas–oil ratio measurements vs. simulation results for A-11H well. Impact of the geomechanical effects upon the bottom-hole pressure—coupled vs. uncoupled models.

The fracture zone parameters determined by the calibration process included its geometrical sizes: its horizontal span of 500 m and vertical extension covering the total thickness of the Ca2 reservoir zone (see Figure 5B).

### 7.2. Model Characterization after Calibration

After the calibration process, the compositional simulation model of the analyzed structure is characterized by the following fundamental parameters:

- Total area of the model:  $234.0 \text{ km}^2 = 15.2 \times 15.3 \text{ km}$ ;
- Model type: single porosity and permeability;
- Lateral dimensions of the model grid:  $160 \times 152 \text{ blocks}$ ;
- Lateral sizes of model blocks:  $100 \times 100 \text{ m}$ ;

- Lateral dimensions of the refined model zone: 5–25 × 100 m;
- Layered structure: 15 layers;
- Number of active blocks: 29,464;
- Initial contact depth:
  - Oil–water contact: 3282 m b.s.l.;
  - Gas–oil contact: 3178 m b.s.l.;
- Initial pressure: 430.2 bar (@ 3282 m b.s.l.);
- Reservoir temperature (constant): 126.8 °C;
- Total model pore volume: 50.84 million m<sup>3</sup>;
- Average values of parameters:
  - Porosity: 9.6%;
  - Horizontal permeability: 52.52 mD;
  - Vertical permeability: 6.37 mD;
  - Average thickness of a single simulation layer: 2.46 m.

## 8. Simulation Results of Production/Injection Forecasts

The calibrated dynamical flow model of the analyzed structure described in the previous sections was utilized to perform simulation forecasts of reservoir behavior for various scenarios including primary production methods and enhanced oil recovery with CO<sub>2</sub> injection, taking into account or neglecting the geomechanical effects and various widths of the fracture zone. The EOR with CO<sub>2</sub> injection scenarios were followed by a CO<sub>2</sub> sequestration stage. The complete set of scenarios presented and discussed in the following sections is listed in Table 6.

**Table 6.** Scenario list of simulation forecasts.

Scenario No.	Scenario Name	Scenario Description		
		Production Method	Geomechanical Effects	Fracture Zone Width (m/Blocks)
1	Basic_w/o_geomechanics_5m_fracture_zone	Primary	Disabled	5/1
2	Basic_w/_geomechanics_5m_fracture_zone	Primary	Enabled	5/1
3	EOR_w/o_geomechanics_5m_fracture_zone	EOR with CO <sub>2</sub> injection *	Disabled	5/1
4	EOR_w/_geomechanics_5m_fracture_zone	EOR with CO <sub>2</sub> injection *	Enabled	5/1
5	EOR_w/o_geomechanics_18m_fracture_zone	EOR with CO <sub>2</sub> injection *	Disabled	18/3
6	EOR_w/_geomechanics_18m_fracture_zone	EOR with CO <sub>2</sub> injection *	Enabled	18/3
7	EOR_w/o_geomechanics_65m_fracture_zone	EOR with CO <sub>2</sub> injection *	Disabled	65/5
8	EOR_w/_geomechanics_65m_fracture_zone	EOR with CO <sub>2</sub> injection *	Enabled	65/5

\* followed by CO<sub>2</sub> sequestration.

### 8.1. Technical and Operational Conditions of Production/Injection Forecasts

The oil production was initially performed by seven existing wells (A-1, A-2K, A-4, A-7H, A-11H, A-13K, and C-2K). In Scenarios 3–8, the CO<sub>2</sub> injection was initially performed by two existing wells (C-1 and C-4). When the producing wells gradually ceased to produce due to the limiting factors listed below, they were converted into injecting ones. As a consequence, the number of producing wells was reduced to one (Scenarios 3 and 5) or zero (Scenarios 4, 6, 7, and 8) at the end of the 15-year interval of the simulated reservoir operation. Similarly, the number of injecting wells increased up to seven in all scenarios. The detailed time variations in these numbers are shown in Figures 14–16 for Scenarios 3 and 4, 5 and 6, and 7 and 8, respectively. In the separate Scenarios 1 and 2 with no CO<sub>2</sub> injection, the numbers of producing wells diminishing with time are shown in Figure 17.

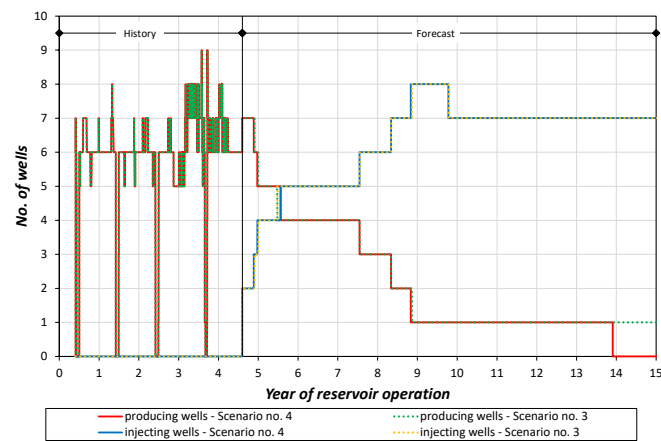


Figure 14. Variation in the number of producing and injecting wells with time. Scenarios 3 and 4.

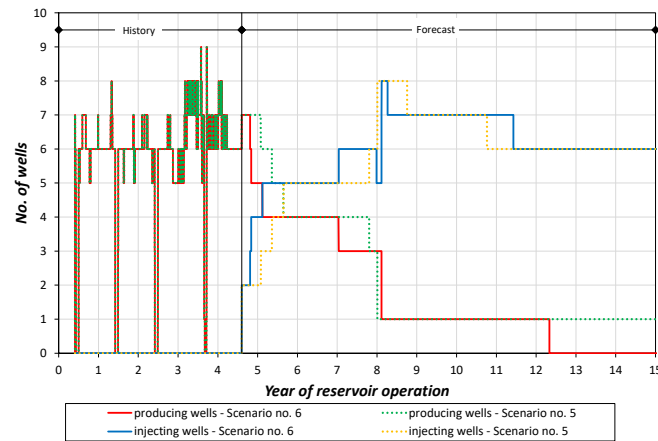


Figure 15. Variation in the number of producing and injecting wells with time. Scenarios 5 and 6.

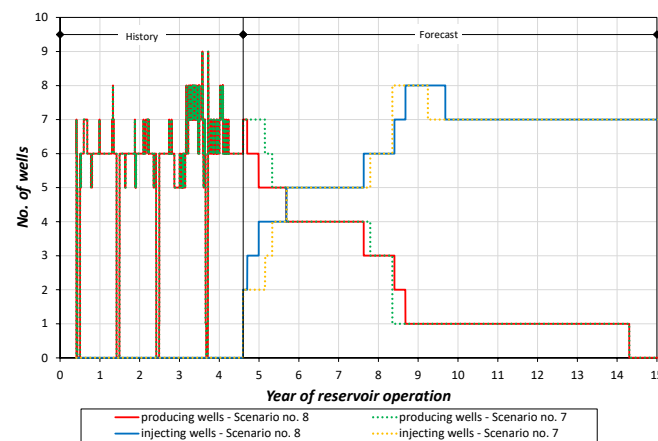


Figure 16. Variation in the number of producing and injecting wells with time. Scenarios 7 and 8.

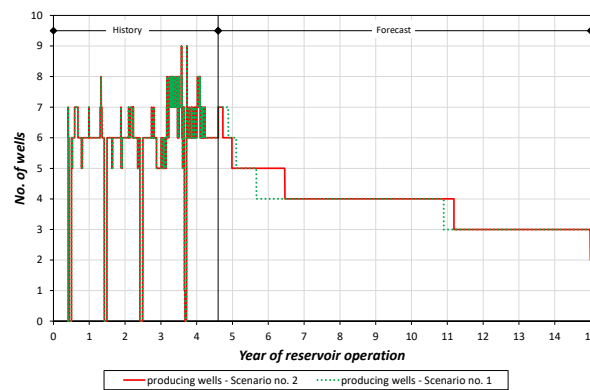


Figure 17. Variation in the number of producing and injecting wells with time. Scenarios 1 and 2.

The oil-producing wells were controlled by production rates estimated as annual average values of the last year’s historical data. The CO<sub>2</sub>-injecting wells were controlled by an injection rate of 500 m<sup>3</sup>/day (where m<sup>3</sup> means cubic meters under reservoir conditions), the value resulting from the operator’s experience. The other production/injection constraints followed the historical restrictions accepted by the reservoir operator, including the following: minimum dynamical bottom-hole pressures, maximum permitted gas–oil ratio and water cut, minimum economic production oil rate, and maximum dynamical bottom-hole pressures at injecting wells. In addition, the reservoir production was also limited by the maximum allowable 3% of CO<sub>2</sub> mole concentration in the total reservoir production stream. When this limit was exceeded, the oil-producing well with the largest contributions of CO<sub>2</sub> production was reduced to obtain the CO<sub>2</sub> concentration of the total production stream below the limit.

8.2. Results at Reservoir Level

The simulation forecast results for the reservoir performance including oil production rates, oil production totals, average reservoir pressures, and (where appropriate) CO<sub>2</sub> injection rates together with CO<sub>2</sub> injection totals are presented in Figures 18–21 for Scenarios 1 and 2, 3 and 4, 5 and 6, and 7 and 8, respectively. The scenarios were grouped in pairs differing in the treatment of geomechanical effects: one neglecting these effects and the other taking them into account. In general, the simulation results at the reservoir level show that the geomechanical effects lead to a small reduction in oil production (below 7% of the total oil production) and a very small increase in CO<sub>2</sub> injection (below 3% of the total CO<sub>2</sub> injection). These variations result from a small contribution of the fracture zone to the total A-11H well productivity/injectivity potential and, as a consequence, to the total reservoir results.

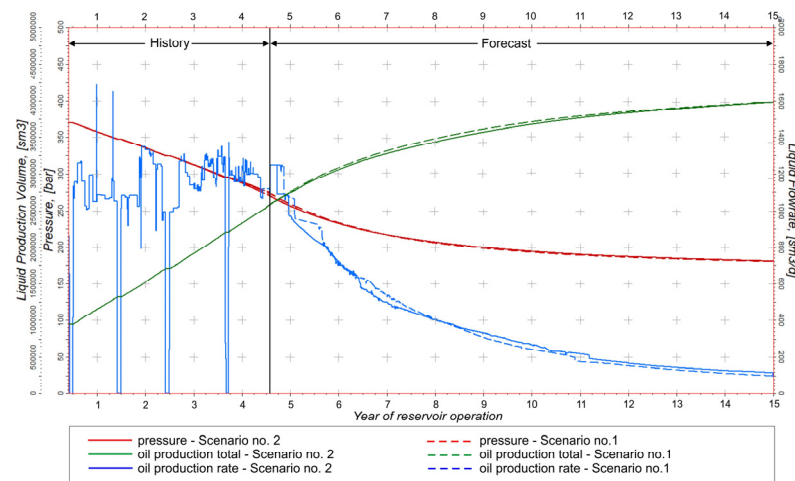


Figure 18. Comparison of basic Scenarios 1 and 2 (see Table 6 for detailed descriptions of the scenarios). Oil production total, oil production rate, and average reservoir pressure.

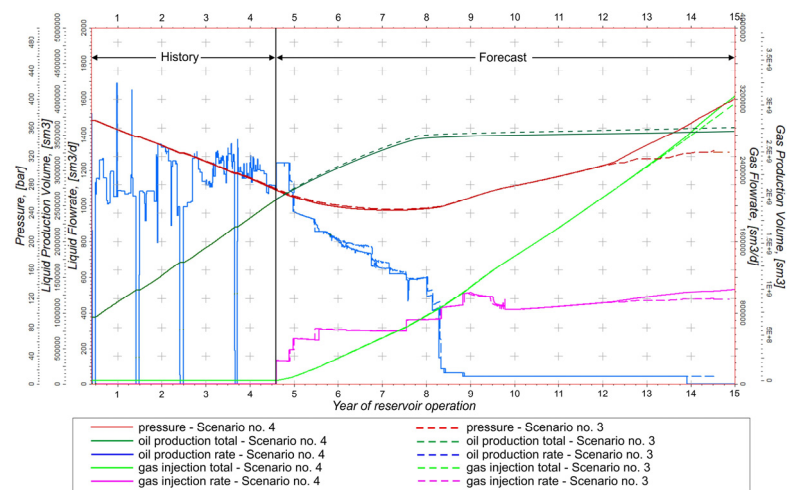


Figure 19. Comparison of EOR Scenarios 3 and 4 (see Table 6 for detailed descriptions of the scenarios). Oil production total, oil production rate, gas injection total, gas injection rate, and average reservoir pressure.

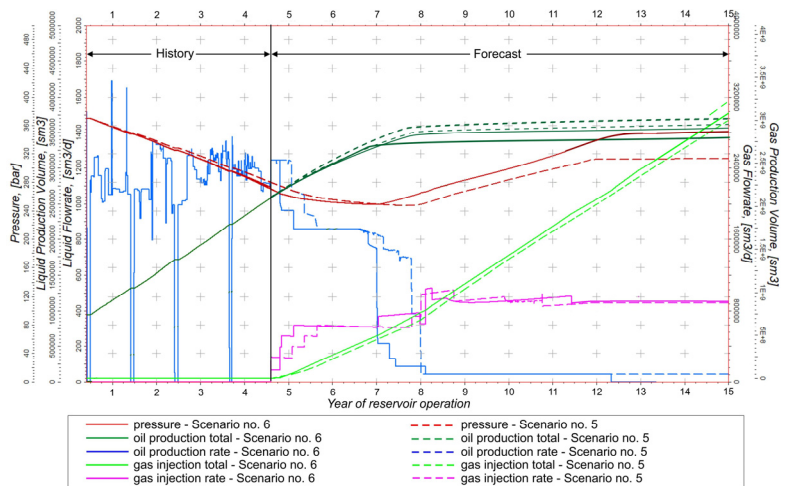


Figure 20. Comparison of EOR Scenarios 5 and 6 (see Table 6 for detailed descriptions of the scenarios). Oil production total, oil production rate, gas injection total, gas injection rate, and average reservoir pressure.

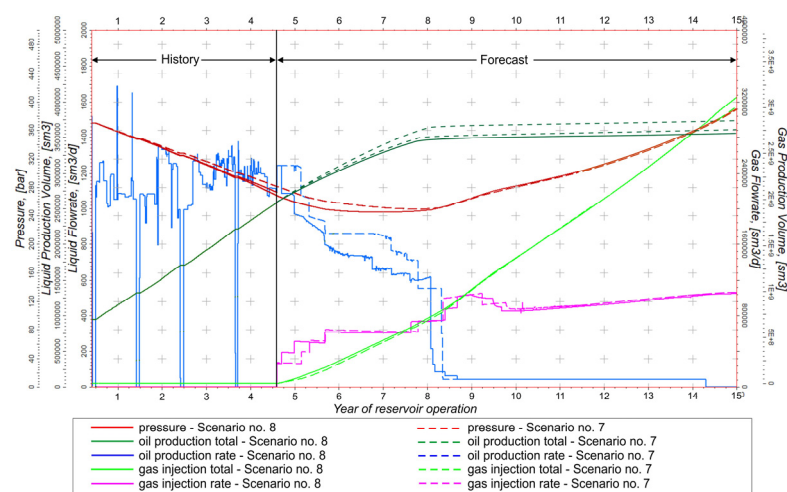
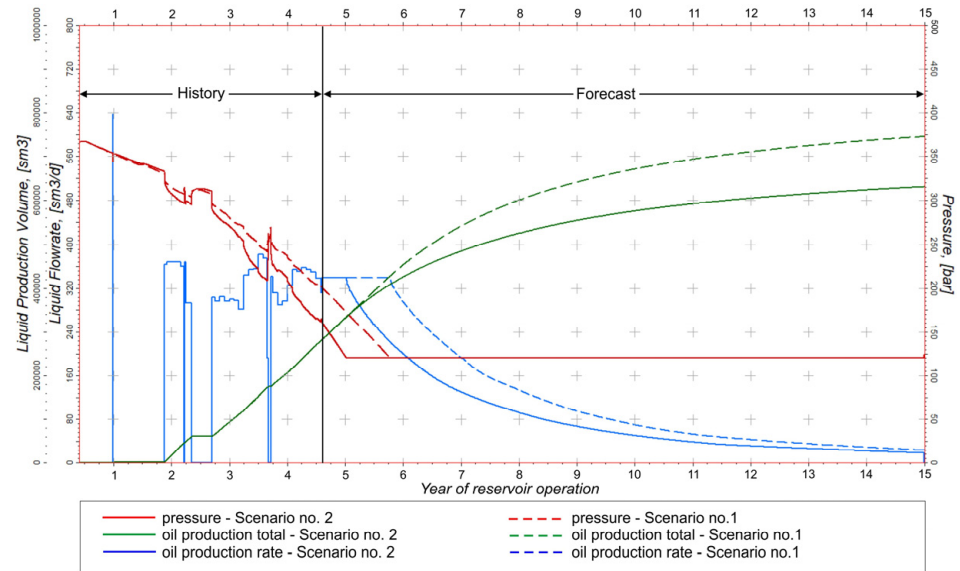


Figure 21. Comparison of EOR Scenarios 7 and 8 (see Table 6 for detailed descriptions of the scenarios). Oil production total, oil production rate, gas injection total, gas injection rate, and average reservoir pressure.

### 8.3. Results at A-11H Well Level

The simulation forecast results for A-11H well including oil production rates, oil production totals, average reservoir pressures, and (where appropriate) CO<sub>2</sub> injection rates together with CO<sub>2</sub> injection totals are presented in Figures 22–25 for Scenarios 1 and 2, 3 and 4, 5 and 6, and 7 and 8, respectively.



**Figure 22.** Comparison of basic Scenarios 1 and 2 (see Table 6 for detailed descriptions of the scenarios). Oil production total, oil production rate, and bottom-hole pressure of A-11H well.

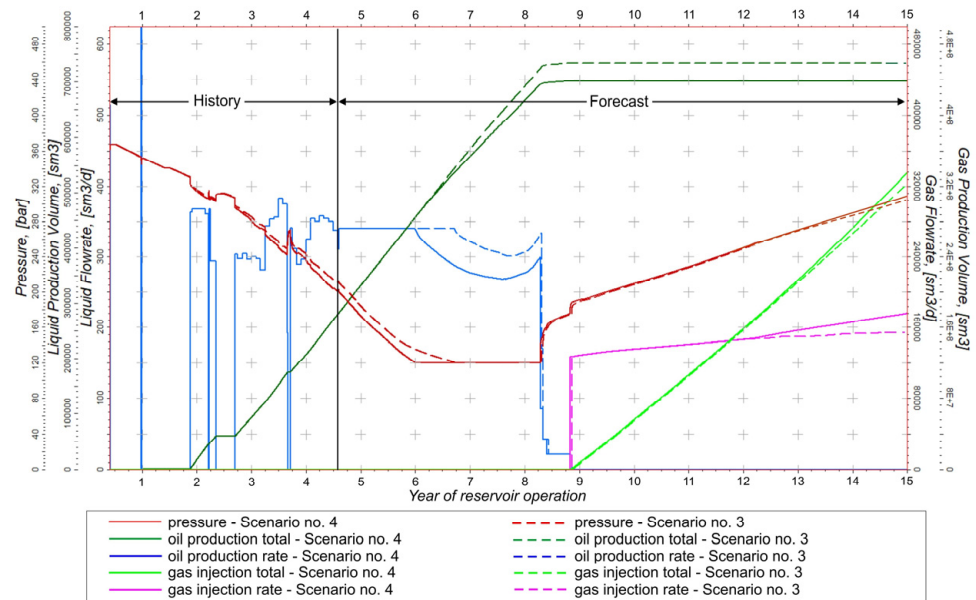


**Figure 23.** Comparison of EOR Scenarios 3 and 4 (see Table 6 for detailed descriptions of the scenarios). Oil production total, oil production rate, gas injection total, gas injection rate, and bottom-hole pressure of A-11H well.

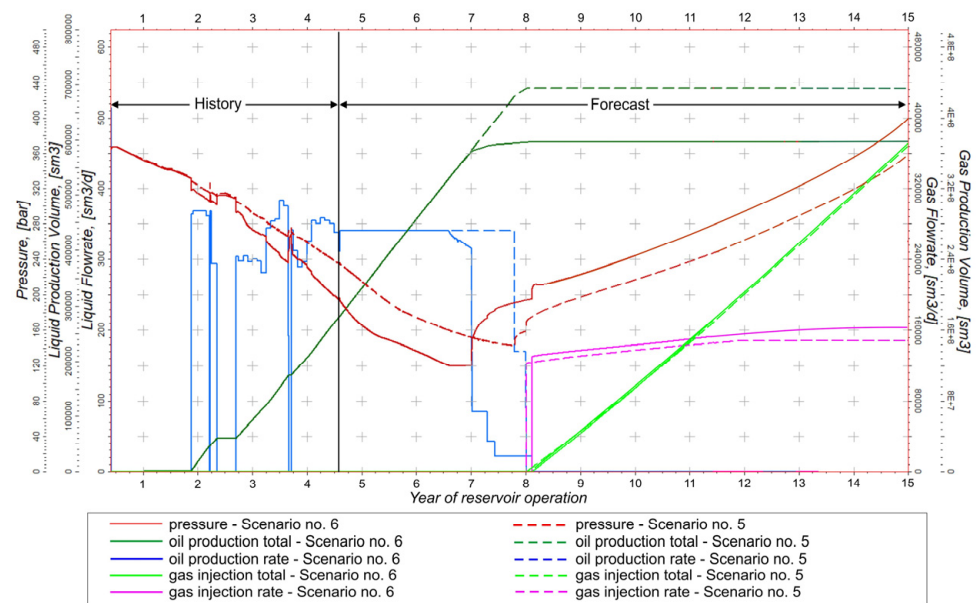


**Figure 24.** Comparison of EOR Scenarios 5 and 6 (see Table 6 for detailed descriptions of the scenarios). Oil production total, oil production rate, gas injection total, gas injection rate, and bottom-hole pressure of A-11H well.

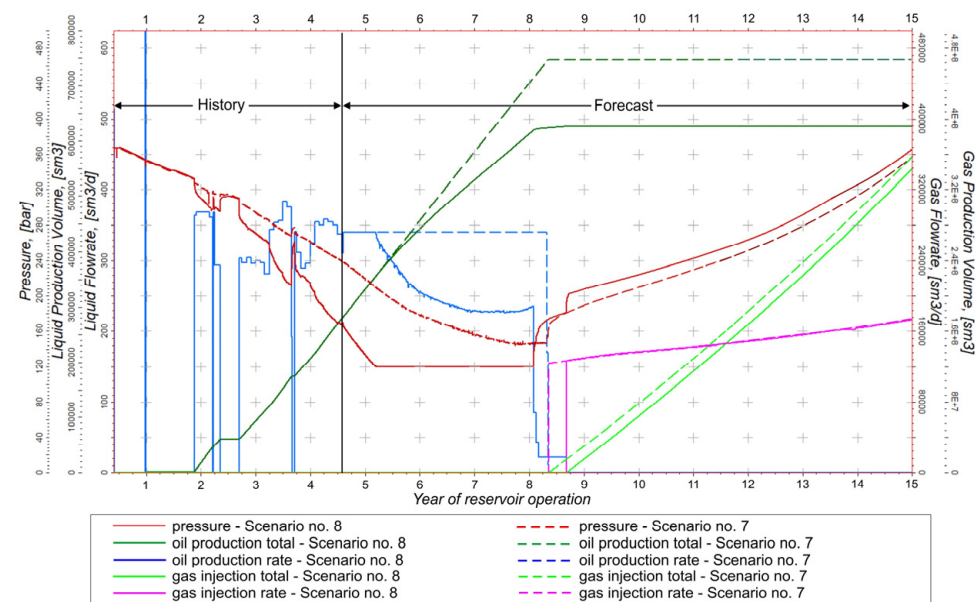


**Figure 25.** Comparison of EOR Scenarios 7 and 8 (see Table 6 for detailed descriptions of the scenarios). Oil production total, oil production rate, gas injection total, gas injection rate, and bottom-hole pressure of A-11H well.

The simulation results for A-11H well provide the following evidence for the significance of the geomechanical effects in both primary and enhanced recovery processes:

- The direct factor determining the geomechanical effects, as well as the oil production, is the reservoir pressure evolution;
- In particular, the injection of the CO<sub>2</sub> makes the reservoir pressure decrease slower and, consequently, maintains the total oil production at a much higher level as can be seen by comparing basic scenarios (Scenario 1 and Scenario 2 of the total oil production after 8<sup>1</sup>/<sub>3</sub> years of operation equal to 0.53 and 0.62 × 10<sup>6</sup> Sm<sup>3</sup>, respectively) with enhanced oil recovery scenarios (Scenario 3 and Scenario 4 of the total oil production

- after  $8^{1/3}$  years of operation equal to  $0.71$  and  $0.77 \times 10^6 \text{ Sm}^3$ , respectively)—the solid and dashed curves in Figure 22 vs. the ones in Figure 23;
- The decrease in the oil production in all the scenarios with the geomechanical effects included due to the fracture closure with pressure decline as can be seen by comparing scenarios with geomechanical effects taken into account (Scenario 1 and Scenario 3 of the total oil production after  $8^{1/3}$  years of operation equal to  $0.53$  and  $0.71 \times 10^6 \text{ Sm}^3$ , respectively) with the scenarios with the geomechanical effects neglected (Scenario 2 and Scenario 4 of the total oil production after  $8^{1/3}$  years of operation equal to  $0.62$  and  $0.77 \times 10^6 \text{ Sm}^3$ , respectively)—the solid curve vs. the dashed one in Figure 22 for the basic scenarios and the solid curve vs. the dashed one in Figure 23 for the enhanced recovery scenarios.

Another variation in the relative differences between oil production totals for scenarios with and without the geomechanical effects can be observed as a function of the fracture zone width. When  $\text{CO}_2$  injection is performed, the geomechanical effects reduce the oil production total by 5%, 14%, and 16% for the fracture zone width of 5, 18, and 65 m, respectively, as shown in Figures 23–25. The larger the width, the bigger the difference, as can be explained by various contributions of the fracture zone to the well productivity. As a result, the geomechanical effects seem to be relatively stronger for scenarios with primary production than for those with  $\text{CO}_2$  injection. It is worth noting that the influence of the geomechanical effects in the fracture zone on the well productivity is partially compensated by the method applied to well control by a nominal production rate. Only when the bottom-hole pressure reaches its minimum level due to the increasing recovery is the production rate reduced to maintain the limiting pressure.

#### 8.4. Results at the Fracture Zone Level

The analogous simulation results referring to the fracture zone of the A-11H well are presented for the same pairs of scenarios in Figures 26–29. They show an impact of the geomechanical effects upon production and injection to be firmly manifested at the level of the zone. The geomechanical effects upon the production stage of the project are already observed in Scenarios 1 and 2, corresponding to the primary production method as presented in Figure 26. Scenario 2, where the geomechanical effects are included, results in a reduction in the oil production total by the approximate factor of 90 (from  $20,000 \text{ sm}^3$  down to  $2180 \text{ sm}^3$ ) due to the apparent closure of the fractures caused by pressure decline following reservoir fluid production—the enhanced effect already pointed out in the discussion of the simulation results at the well level.

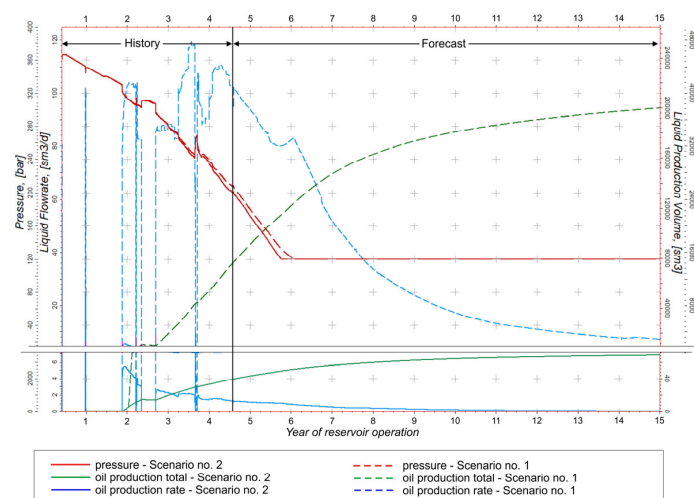


**Figure 26.** Comparison of basic Scenarios 1 and 2 (see Table 6 for detailed descriptions of the scenarios). Oil production total and rate of the fracture zone at A-11H well, bottom-hole pressure at the fracture zone connection with A-11H well.

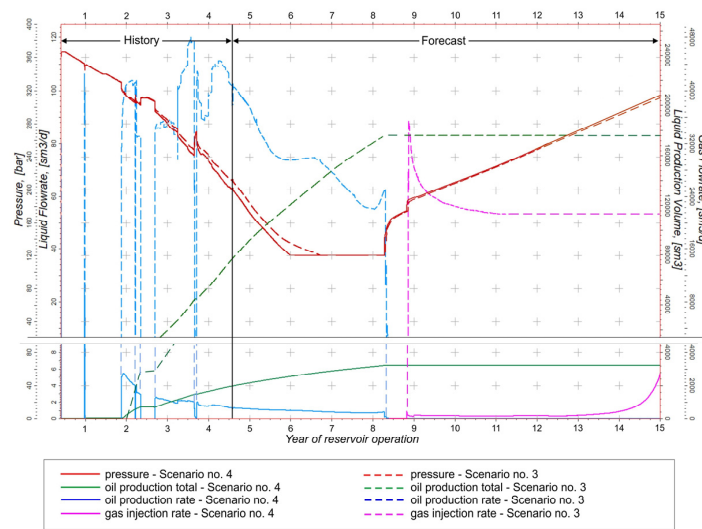


**Figure 27.** Comparison of EOR Scenarios 3 and 4 (see Table 6 for detailed descriptions of the scenarios). Oil production total and oil production rate of the fracture zone at A-11H well. CO<sub>2</sub> injection total and CO<sub>2</sub> injection rate of the fracture zone at A-11H well. Bottom-hole pressure at the fracture zone connection with A-11H well.

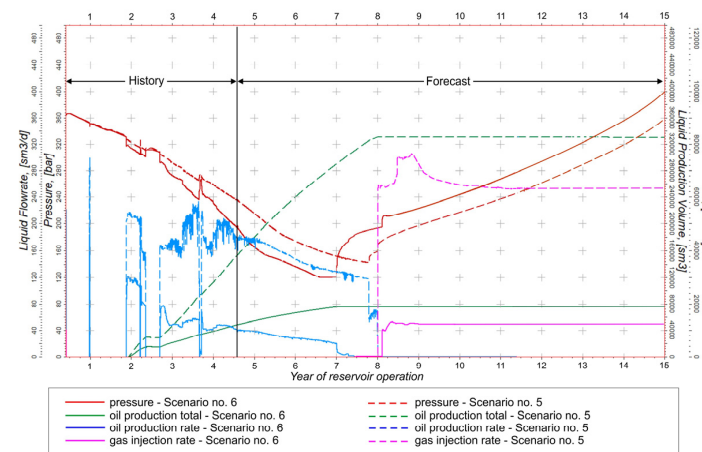


**Figure 28.** Comparison of EOR Scenarios 5 and 6 (see Table 6 for detailed descriptions of the scenarios). Oil production total and oil production rate of the fracture zone at A-11H well. CO<sub>2</sub> injection total and CO<sub>2</sub> injection rate of the fracture zone at A-11H well. Bottom-hole pressure at the fracture zone connection with A-11H well.

The oil production rates and totals drastically fall during the production stage due to the fracture closure caused by the decreasing pressure for both the basic production scheme (the solid green curve vs. the dashed green one in Figure 26 for the total production reduction factor of 0.0003) and the EOR production method (the solid green curve vs. the dashed green one in Figure 27 for the total production reduction factor of 0.018). Unexpectedly, the CO<sub>2</sub> injection rate increases very slowly, despite a rise in the bottom-hole pressure, and the injection of Scenario 3 including the geomechanical effects never reaches that of Scenario 4, i.e., the one without the geomechanical effects. Similar conclusions refer to Scenario 5 vs. Scenario 6 and Scenario 7 vs. Scenario 8. The slight rise in the CO<sub>2</sub> injection rate during the sequestration stage is a result of the combination of several factors. When the injection stage is started, the injection gas saturation at the fracture zone connection with the well rises rapidly to its maximum level. That implies a rapid increase in the relative permeability of the injection phase and a constant increase in the injectivity index at the fracture zone scale. As a consequence, it can be inferred that the effective

resistivity between the fracture zone and the well is relatively small when comparing it to the resistivity of the reservoir section around the wellbore itself. The effective resistivity of the near-wellbore reservoir initially dominates the injection process but decreases much slower than the effective resistivity of the fracture zone. Finally, the total resistivity of the reservoir system produces a delayed effect of the injection rate enhancement at the fracture zone level. Such an effect is most evident in cases of the scenarios with the geomechanics enabled and the fracture zone width of 5 m presented in Figure 27.

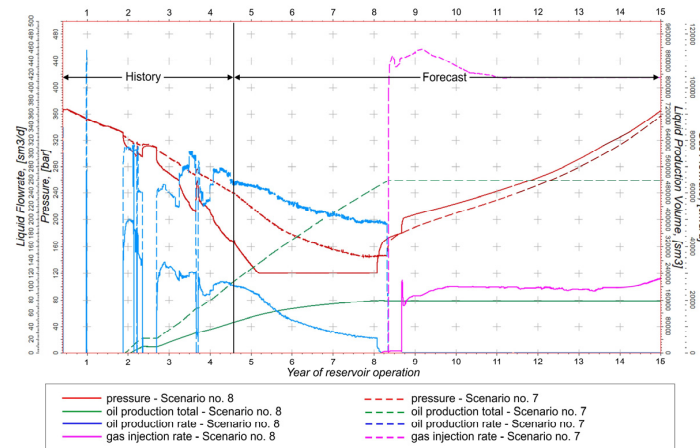


**Figure 29.** Comparison of EOR Scenarios 7 and 8 (see Table 6 for detailed descriptions of the scenarios). Oil production total and oil production rate of the fracture zone at A-11H well. CO<sub>2</sub> injection total and CO<sub>2</sub> injection rate of the fracture zone at A-11H well. Bottom-hole pressure at the fracture zone connection with A-11H well.

When variations in the fracture zone width are taken into account, another phenomenon can be noticed. When the fracture zone width increases, so does the total oil production separately for both the cases neglecting the geomechanical effects ( $176, 332,$  and  $520 \times 10^3 \text{ Sm}^3$  for 5, 18, and 65 m width fracture zone, respectively; the dashed green curves in Figures 27–29) and the cases including those effects ( $3.25, 68,$  and  $160 \times 10^3 \text{ Sm}^3$  for 5, 18, 65 m width fracture zone, respectively; the solid green curves in Figures 27–29). Hence, the total oil production dependence upon the fracture zone width for cases neglecting the geomechanical effects is larger than the analogous dependence for cases including the geomechanical effects. As a consequence, a rather unexpected conclusion follows: the geomechanical effects reduce the oil production total by a relatively higher degree for a narrower fracture zone than for a wider one, i.e., by a factor of 67, 7.0, and 6.4 (from 20%, 35%, and 58% down to 0.3%, 5%, and 9%) for the fracture zone width of 5, 18, and 65 m, respectively (the solid vs. dashed green curves in Figures 27–29). The corresponding results are shown collectively in Figure 30.

Similar behavior can be observed in the contribution of the fracture zone to the injectivity of A11-H well—reduction in this fracture zone contribution due to the geomechanical effects is reported as follows: by a factor of 10, 4.9, and 4.6 (from 15%, 44%, and 73% down to 1.5%, 9%, and 16%) for 5, 18, and 65 m width of the fracture zone, respectively (the corresponding results are shown in Figure 30). Despite the increasing bottom-hole pressure during the injection period of the CO<sub>2</sub>-EOR and CO<sub>2</sub> sequestration, the fracture zone reveals reduced injectivity due to the effects of partial fracture closure.

The fracture zone is analyzed for cases with its widths increasing geometrically: from 5 m through 18 m up to 65 m. This variation entails a nonlinear change in the production and injection results between the corresponding scenarios. The rise in the fracture zone width by the factor of 3.6 (from 5 m to 18 m) causes an almost double (by a factor of 1.75) increase in the zone contribution to the well oil production and an almost triple (by a factor of 2.9) increase in the zone contribution to the well gas injection for the scenarios neglecting geomechanical effects. In scenarios with the geomechanical effects, the zone contribution

to the well oil production rises about 16 times and the zone contribution to the well gas injection rises 6 times. When the fracture zone width increases by the subsequent factor of 3.6 (from 18 m to 65 m), the zone contribution to the well oil production/CO<sub>2</sub> injection rises by 1.7 times for the former scenarios. When taking into account the latter scenarios, the zone contribution to the well oil production/CO<sub>2</sub> injection rises by a factor of 1.8, as can be deduced from the results presented in Figure 30.

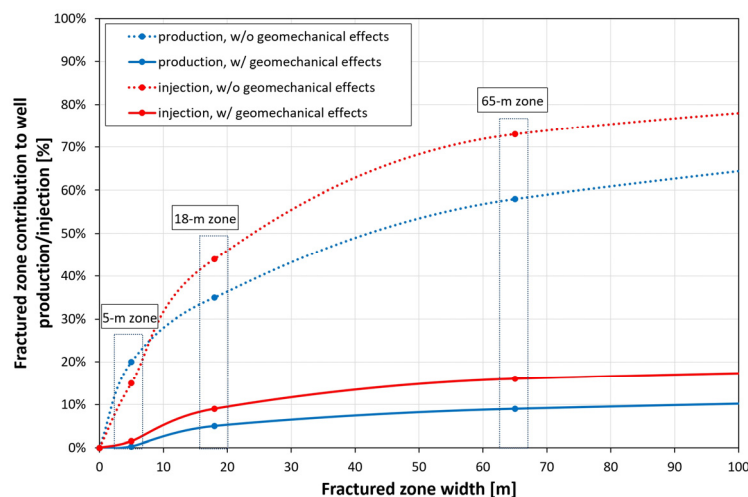


**Figure 30.** Fracture zone contribution to total A11-H well production/injection vs. various fracture zone widths.

The geomechanical effects resulted in much larger differences in the oil production for the scenarios with primary production than for those with CO<sub>2</sub> injection. It is worth adding that the influence of the geomechanical effects in the fracture zone on the well productivity is partially compensated by the method of well control applying a nominal production rate. Only when the bottom-hole pressure reaches its minimum level due to decreased productivity is the production rate reduced to maintain the limiting pressure.

## 9. Fracture Propagation Analysis

To maintain the secure storage of CO<sub>2</sub> in the analyzed reservoir formation after reaching the maximum CO<sub>2</sub> allowance of the production wells, the integrity of the basal anhydrite A2—a sealing formation—has to be preserved [105]. Under the condition of the pre-existing fracture zone within the reservoir rock, the analysis of possible fracture propagation is critical.

For tracking the changes in the fracture zone vicinity, indicative parameters suggesting whether the fracture is propagating were used: failure mode, normal effective stress, and normal strain as resulted from geomechanical simulations calculated for particular time steps of the field production, application of CO<sub>2</sub>-EOR method, and CO<sub>2</sub> sequestration.

To determine fracture propagation, a commonly used Mohr–Coulomb criterion was used with a tension cut-off [106–108]. The vicinity of the modeled fracture within the reservoir rock and directly overlying caprock (Figure 29) did not meet the failure criteria (Figure 29) and remained intact through the analyzed stages of CO<sub>2</sub> injection [105]. In Figure 29, a Mohr–Coulomb diagram is shown, which is plotted for the grid cells located right above the top reservoir showing no signs of rock failure.

What is more, the results of geomechanical simulations revealed positive values of the normal stress and strain (Figure 31C,D, respectively), indicating no sign of tensile strain at the fracture zone and in its close vicinity, especially in the overlying basal anhydrite A2, suggesting, therefore, no fracture propagation [109] and the lack of rock failure.

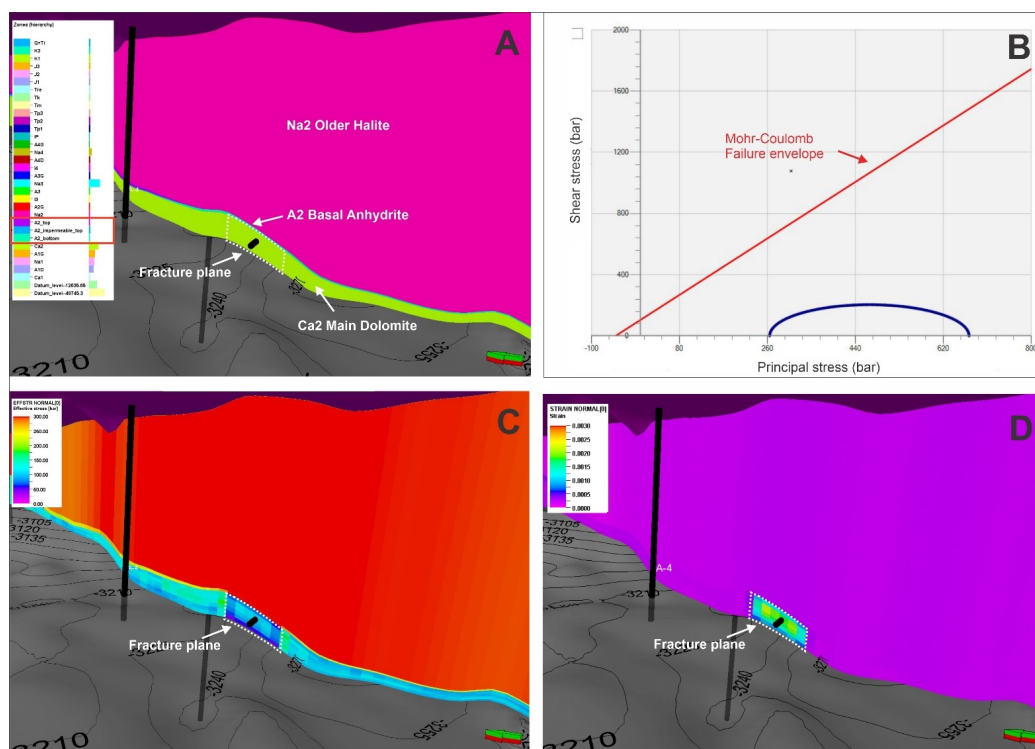


**Figure 31.** Characterization of fracture zone and its vicinity (A) in terms of fracture propagation indicators: (B) Mohr–Coulomb diagram for the A2 basal anhydrite caprock; 3D distribution of normal effective stress (C) and normal strain (D).

The indicators mentioned above suggest a lack of failure and no further fracture propagation at the analyzed stages of CO<sub>2</sub> injection.

All the above parameters confirmed no lateral or vertical propagation of the fracture zone during the history of hydrocarbon production and CO<sub>2</sub> injection to the reservoir.

## 10. Summary and Conclusions

The studies described in this paper address the problem of geomechanical effects and their influence on the modeling of oil production and CO<sub>2</sub> injection (CO<sub>2</sub>-EOR followed by CO<sub>2</sub> sequestration). The studies are focused on natural fracture geomechanics and its results for the reservoir, well, and completion performance. The paper includes methods, assumptions, and results of these studies as applied to the geological structure of a domestic oil reservoir that is a potential object for CO<sub>2</sub>-EOR method application as well as a facility for a CO<sub>2</sub> sequestration project.

In particular, an analysis was performed for the transport properties of an induced fracture zone as a function of its geomechanical state as well as the state of its neighborhood.

For this purpose, 3D geological structural and parametric models were constructed and implemented in a dynamical flow model and a static geomechanical one for both flow and geomechanical simulations. An effective method of direct dependence between pore pressure variation and basic geological parameter variation via the geomechanical parameter changes was employed in this study. By identifying separate regions of a uniform variation in geomechanical state parameters with reservoir pressure changes during continuity intervals, specific correlations are found for basic parameters (porosity, permeability) as direct functions of pressure in various reservoir regions and time intervals.

The constructed reservoir model of the analyzed structure, including the oil reservoir, screening caprocks, and other surrounding formations, was satisfactorily calibrated based on the data obtained from the reservoir operator and covering 16 years of its operation with 11 producing wells.

The calibrated reservoir model effectively coupled with geomechanical effects was utilized to perform simulation forecasts of reservoir behavior for various scenarios including primary production methods, enhanced oil recovery with CO<sub>2</sub> injection followed by CO<sub>2</sub> sequestration, and various extensions (widths) of the fracture zone.

The studies performed within the reported research allow us to draw the following conclusions:

General conclusions are as follows:

1. The method proposed in the studies and comprising effectively coupled geomechanical and dynamical simulations of reservoir region and its extension allows us to take into account the influence of geomechanical effects upon transport properties of reservoir rock and, consequently, upon the operation of the reservoir in various stages including primary production, enhanced oil production by CO<sub>2</sub> injection, and CO<sub>2</sub> sequestration;
2. The geomechanical effects induced primarily by the redistribution of reservoir pressure may drastically modify transport properties of fracture zones contributing to well performance and thus determining the operational results of the involved reservoir;
3. The quantitative results of those geomechanical effects depend upon detailed properties of both geomechanical state evolution and geological characteristics of the reservoir;
4. The following two correlations are key factors when the effective transport properties of the reservoir rock are a concern:
  - The correlation between the geomechanical state (stress and strain field) and the rock pore matrix and fracture characteristics;
  - The correlation between pore matrix/fracture characteristics and their effective transport properties.

Conclusions specific to the analyzed geological structure are as follows:

1. Assumed geometries of discontinuities and the reservoir stress field indicate that fractures are reactivated in tensile/hybrid failure mode caused by pressure build-up during CO<sub>2</sub> injection; induced aperture changes result from the normal stress while the shear stress can be neglected;
2. Under the geomechanical stress state resulting from the simulations of both production and injection stages of the reservoir operation, the fracture zone will not propagate within the underlying main dolomite formation or the anhydrite caprock; hence, no CO<sub>2</sub> leakage upward into the anhydrite formation via induced fractures is observed;
3. The geomechanical effects significantly determine simulation forecasts of oil production by an oil-producing well with completion including a fracture zone, and the pressure reduction results in fracture closure and a reduction in the fracture contribution to the well productivity depending on the size of the fractured zone;
4. The productivity reduction of the fracture zone alone may be as large as 60-fold (Figure 24) for primary production with a narrow fracture zone and 3-fold for the CO<sub>2</sub>-EOR production method with a wider fracture zone (Figure 27);
5. Similar results for geomechanical effects are found in well injectivity due to fracture apertures not regaining their primary size despite the increasing reservoir pressure during the injection phase of the CO<sub>2</sub>-EOR and CO<sub>2</sub> sequestration;
6. In the cases of carbonate reservoir rocks with more frequent fracture occurrences, the evaluated geomechanical effects in the field performance are expected to be enhanced at the reservoir scale.

**Author Contributions:** Conceptualization, W.S. and M.S.-V.; methodology, W.S. and M.S.-V.; software, P.R. and K.S.; validation, W.S. and K.S.; formal analysis, P.R. and M.S.-V.; investigation, P.R. and M.S.-V.; resources, P.R. and K.S.; data curation, P.R. and M.S.-V.; writing—original draft preparation, W.S. and M.S.-V.; writing—review and editing, K.S.; visualization, P.R. and M.S.-V.; supervision, W.S.; project administration, K.S. All authors have read and agreed to the published version of the manuscript.

**Funding:** This research was carried out as part of the following project: Evaluation of the impact of fractures presence on the efficiency of CO<sub>2</sub>-EOR as well as the sequestration capacity and tightness of

the geological structure, which is funded by the Polish Ministry of Science and Higher Education, Grant No. DK-4100-106/21. The authors would like to express their gratitude to the Polish Ministry of Science and Higher Education for funding this research.

**Data Availability Statement:** 3rd Party Data. Restrictions apply to the availability of these data. Data was obtained from Polish Oil and Gas Company and are available from the authors with the permission of Polish Oil and Gas Company.

**Conflicts of Interest:** The authors declare no conflict of interest.

## Nomenclature

$b$	equivalent normal closure aperture;
$b_{max}$	maximum aperture;
$b_r$	residual aperture;
$d$	equivalent shear dilation aperture;
$d_{max}$	maximum shear dilation;
$E$	Young modulus;
$E_{dyn}$	dynamic Young modulus;
$f_d$	equivalent shear dilation frequency;
$f_n$	equivalent fracture frequency;
$p$	pore pressure;
$q$	equivalent frictional coefficient;
$T$	tensile strength;
$\nu$	Poisson's ratio;
$\nu_{dyn}$	dynamic Poisson's ratio;
$v_p$	compressional wave velocity;
$v_s$	shear wave velocity;
$\alpha$	Biot's coefficient;
$\alpha'$	stress coefficient for the normal closure aperture;
$\sigma_h$	minimum horizontal stress;
$\sigma_H$	maximum horizontal stress;
$\sigma_{max}$	maximum principal stress in the plane perpendicular to the fracture surface;
$\sigma_{min}$	minimum principal stress in the plane perpendicular to the fracture surface;
$\sigma_r$	ratio of maximum principal stress;
$\sigma_v$	vertical stress;
$\gamma$	stress coefficient for shear dilation;
$\varepsilon_H$	tectonic strains parallel to the maximum horizontal stress direction;
$\varepsilon_h$	tectonic strains parallel to the minimum horizontal stress direction;
$\rho$	rock density.

## References

1. Azzolina, N.; Gorecki, C.; Pu, H.; Peck, W.; Ayash, S.; Melzer, S.; Nakles, D.; Chatterjee, S. Statistical analysis of CO<sub>2</sub> EOR production and injection data to examine ongoing and ultimate CO<sub>2</sub> EOR incidental storage. In Proceedings of the Thirteenth Annual Conference on Carbon Capture, Utilization & Storage Conference, Pittsburgh, PA, USA, 28 April–1 May 2014; David L. Lawrence Convention Center: Pittsburgh, PA, USA, 2014. 20p.
2. Ghedan, S. Global Laboratory Experience of CO<sub>2</sub>-EOR Flooding. In Proceedings of the 2009 SPE/EAGE Reservoir Characterization and Simulation Conference, Abu Dhabi, United Arab Emirates, 19–21 October 2009; Society of Petroleum Engineers: Richardson, TX, USA, 2009. 15p. [[CrossRef](#)]
3. Holm, L. Carbon Dioxide Solvent Flooding for Increased Oil Recovery. *Trans. AIME* **1959**, *216*, 225–231. [[CrossRef](#)]
4. Jarrell, P.M.; Fox, C.E.; Stein, M.H.; Webb, S.L. *Practical Aspects of CO<sub>2</sub> Flooding*; Society of Petroleum Engineers Monograph Series, v. 22; Society of Petroleum Engineers: Richardson, TX, USA, 2002; 220p, ISBN 978-1-55563-096-6. [[CrossRef](#)]
5. Martin, D.F.; Taber, J.J. Carbon Dioxide Flooding. *J. Pet. Technol.* **1992**, *44*, 396–400. [[CrossRef](#)]
6. Mungan, N. Carbon Dioxide Flooding—Fundamentals. In *Heavy Crude Oil Recovery*; Springer: Dordrecht, The Netherlands, 1981; pp. 87–92, ISBN 978-94-009-6140-1. [[CrossRef](#)]
7. Peng, B. *CO<sub>2</sub> Storage in the Oil Reservoir and Enhanced Oil Recovery*; University of Petroleum, Enhanced Oil Recovery Research Center: Beijing, China, 11–15 July 2011; 39p.
8. Remson, D. *Storing CO<sub>2</sub> and Producing Domestic Crude Oil with Next-Generation CO<sub>2</sub>-EOR Technology*; DOE/NETL-2010/1417; National Energy Technology Laboratory: Albany, OR, USA, April 2010; 59p.

9. Tzimas, E.; Georgakaki, A.; Cortes, C.G.; Peteves, S.D. *Enhanced Oil Recovery Using Carbon Dioxide in the European Energy System*; Report EUR 21895 EN, European Commission, Directorate General Joint Research Centre (DG JRC); Institute of Energy: Petten, The Netherlands, December 2005; 118p, ISBN 92-79-01044-1, EUR 21895 EN, JRC32102.
10. Bradshaw, J.; Rigg, A. The GEODISC Program: Research into Geological Sequestration of CO<sub>2</sub> in Australia. *Environ. Geosci.* **2001**, *8*, 166–176. [[CrossRef](#)]
11. Streit, J.E.; Siggins, A.F. Predicting, monitoring and controlling geomechanical effects of CO<sub>2</sub> injection. In *Greenhouse Gas Control Technologies, Proceedings of the 7th International Conference on Greenhouse Gas Control Technologies, Vancouver, BC, Canada, 5–9 September 2004*; Rubin, E.S., Keith, D.W., Gilboy, C.F., Eds.; Elsevier: Oxford, UK, 2005; pp. 643–651, ISBN 0-08-044881-X, TRN: 000600155.
12. Islam, M.; Chakma, A. Storage and utilization of CO<sub>2</sub> in petroleum reservoirs—A simulation study. *Energy Convers. Manag.* **1993**, *34*, 1205–1212. [[CrossRef](#)]
13. Bachu, S. Sequestration of CO<sub>2</sub> in geological media: Criteria and approach for site selection in response to climate change. *Energy Convers. Manag.* **2000**, *41*, 953–970. [[CrossRef](#)]
14. Koide, H.; Tazaki, Y.; Noguchi, Y.; Nakayama, S.; Iijima, M.; Ito, K.; Shindo, Y. Subterranean containment and long-term storage of carbon dioxide in unused aquifers and in depleted natural gas reservoirs. *Energy Convers. Manag.* **1992**, *33*, 619–626. [[CrossRef](#)]
15. Ennis-King, J.; Paterson, L. Reservoir engineering issues in the geological disposal of carbon dioxide. In *Greenhouse Gas Control Technologies: Proceedings of the 5th International Conference on Greenhouse Gas Control Technologies*; Williams, D.J., Durie, R.A., McMullan, P., Paulson, C.A.J., Smith, A.Y., Eds.; CSIRO Publishing: Cairns, Australia, 2001; pp. 290–295, ISBN 0-643-06672-1, TRN: 000900074.
16. Al-Masri, W.; Papaspyrou, C.; Shapiro, A.; Suicmez, V. Study of the Feasibility of the Carbon Dioxide Injection in a North Sea Petroleum Reservoir. In Proceedings of the SPE Europec Featured at 80th EAGE Conference and Exhibition, Copenhagen, Denmark, 11–14 June 2018. [[CrossRef](#)]
17. Etehadtavakkol, A.; Lake, L.W.; Bryant, S.L. CO<sub>2</sub>-EOR and storage design optimization. *Int. J. Greenh. Gas Control* **2014**, *25*, 79–92. [[CrossRef](#)]
18. Ghomian, Y.; Sepehrnoori, K.; Pope, G.A. Efficient Investigation of Uncertainties in Flood Design Parameters for Coupled CO<sub>2</sub> Sequestration and Enhanced Oil Recovery. In Proceedings of the SPE International Conference on CO<sub>2</sub> Capture, Storage, and Utilization, New Orleans, LA, USA, 10–12 November 2010. [[CrossRef](#)]
19. Safi, R.; Agarwal, R.K.; Banerjee, S. Numerical simulation and optimization of CO<sub>2</sub> utilization for enhanced oil recovery from depleted reservoirs. *Chem. Eng. Sci.* **2016**, *144*, 30–38. [[CrossRef](#)]
20. Arnaut, M.; Vulin, D.; Lamberg, G.J.G.; Jukić, L. Simulation Analysis of CO<sub>2</sub>-EOR Process and Feasibility of CO<sub>2</sub> Storage during EOR. *Energies* **2021**, *14*, 1154. [[CrossRef](#)]
21. Karimaie, H.; Nazarian, B.; Aurdal, T.; Nøkleby, P.H.; Hansen, O. Simulation Study of CO<sub>2</sub> EOR and Storage Potential in a North Sea Reservoir. *Energy Procedia* **2017**, *114*, 7018–7032. [[CrossRef](#)]
22. Liu, Y.; Rui, Z. A Storage-Driven CO<sub>2</sub> EOR for a Net-Zero Emission Target. *Engineering* **2022**, *18*, 79–87. [[CrossRef](#)]
23. Liu, Y.; Rui, Z.; Yang, T.; Dindoruk, B. Using propanol as an additive to CO<sub>2</sub> for improving CO<sub>2</sub> utilization and storage in oil reservoirs. *Appl. Energy* **2022**, *311*, 118640. [[CrossRef](#)]
24. Zhao, X.; Rui, Z.; Liao, X. Case studies on the CO<sub>2</sub> storage and EOR in heterogeneous, highly water-saturated, and extra-low permeability Chinese reservoirs. *J. Nat. Gas Sci. Eng.* **2016**, *29*, 275–283. [[CrossRef](#)]
25. Teklu, T.W.; Alameri, W.; Graves, R.M.; Tutuncu, A.N.; Kazemi, H.; Alsumaiti, A.M. Geomechanics Considerations in Enhanced Oil Recovery. In Proceedings of the SPE Canadian Unconventional Resources Conference, Calgary, AB, Canada, 30 October–1 November 2012. [[CrossRef](#)]
26. Correa, A.C.F.; Newman, R.B.; Naveira, V.P.; de Souza, A.L.S.; Araujo, T.; da Silva, A.A.C.; Soares, A.C.; Herwanger, J.V.; Meurer, G.B. Integrated Modeling for 3D Geomechanics and Coupled Simulation of Fractured Carbonate Reservoir. In Proceedings of the OTC Brasil, Rio de Janeiro, Brazil, 29–31 October 2013. [[CrossRef](#)]
27. Jabbari, H.; Ostadhassan, M.; Salehi, S. Geomechanical Modeling in CO<sub>2</sub> Enhanced Oil Recovery. In Proceedings of the 49th U. S. Rock Mechanics/Geomechanics Symposium, San Francisco, CA, USA, 28 June–1 July 2015. ARMA-2015-262.
28. Elyasi, A.; Goshtasbi, K.; Hashemolhosseini, H.; Barati, S. Coupled solid and fluid mechanics simulation for estimating optimum injection pressure during reservoir CO<sub>2</sub>-EOR. *Struct. Eng. Mech.* **2016**, *59*, 37–57. [[CrossRef](#)]
29. Rahman, J.; Fawad, M.; Mondol, N.H. 3D Field-Scale Geomechanical Modeling of Potential CO<sub>2</sub> Storage Site Smeaheia, Offshore Norway. *Energies* **2022**, *15*, 1407. [[CrossRef](#)]
30. Chiamonte, L.; Zoback, M.D.; Friedmann, J.; Stamp, V. Seal integrity and feasibility of CO<sub>2</sub> sequestration in the Teapot Dome EOR pilot: Geomechanical site characterization. *Environ. Geol.* **2007**, *54*, 1667–1675. [[CrossRef](#)]
31. White, J.A.; Chiamonte, L.; Ezzedine, S.; Foxall, W.; Hao, Y.; Ramirez, A.; McNab, W. Geomechanical behavior of the reservoir and caprock system at the In Salah CO<sub>2</sub> storage project. *Proc. Natl. Acad. Sci. USA* **2014**, *111*, 8747–8752. [[CrossRef](#)]
32. Sharma, P.; Ghosh, S.; Tandon, A. Study of CO<sub>2</sub> injection in a depleted oil reservoir using geomechanically coupled and non-coupled simulation models. *Mater. Today Proc.* **2022**, *57*, 1805–1812. [[CrossRef](#)]
33. Chadwick, A.; Arts, R.; Bernstone, C.; May, F.; Thibeau, S.; Zweigel, P. *Best Practice for the Storage of CO<sub>2</sub> in Saline Aquifers, Observations and Guidelines from the SACS and CO<sub>2</sub> STORE Projects*; British Geological Survey Halstan & Co. Ltd.: Amersham, UK, 2008; ISBN 978-0-85272-610-5.

34. Jia, C.-J.; Xu, W.-Y.; Wang, H.-L.; Wang, R.-B.; Yu, J.; Yan, L. Stress dependent permeability and porosity of low-permeability rock. *J. Cent. South Univ.* **2017**, *24*, 2396–2405. [[CrossRef](#)]
35. Wójcicki, A. *Realization Status and Prospects for the National Program. Assessment of Geological Formations and Structures for Safe Geological Storage of CO<sub>2</sub>, with the Monitoring Program*; Prace Naukowe Instytutu Nafty i Gazu Państwowego Instytutu Badawczego: Kraków, Poland, 2013; Volume 170, pp. 361–365.
36. Davies, P.B. *Evaluation of the Role of Threshold Pressure in Controlling Flow of Waste-Generated Gas into Bedded Salt at the Waste Isolation Pilot Plant*; Sandia Report prepared for the United States Department of Energy under Contract DE-AC04-76DP00789; Sandia National Laboratories: Albuquerque, NM, USA, 1991; Volume 23, pp. 17–19, RN: 23009058.
37. Ibrahim, M.A.; Tek, M.R.; Katz, D.L. *Threshold Pressure in Gas Storage*; American Gas Association, Inc.: Arlington, VA, USA, 1970; ISBN 9780318127248.
38. Tarkowski, R.; Stopa, J. Tightness of geological structure destined for underground carbon dioxide storage. *Gospod. Surowcami Miner.* **2007**, *23*, 129–137.
39. Settari, A.; Mounts, F.M. A Coupled Reservoir and Geomechanical Simulation System. *SPE J.* **1998**, *3*, 219–226. [[CrossRef](#)]
40. Settari, A.; Price, T.R.; Yee, C.T. Coupling of Fluid Flow and Soil Behavior to Model Injection into Unconsolidated Oil Sands. In Proceedings of the 1988 Petroleum Society of CIM Annual Technical Meeting, Calgary, AB, Canada, 12–16 June 1988; CIM 88-39-72.
41. Minkoff, S.E.; Stone, C.M.; Arguello, J.G.; Bryant, S.; Eaton, J.; Peszynska, M.; Wheeler, M. Staggered in Time Coupling of Reservoir Flow Simulation and Geomechanical Deformation: Step 1—One-Way Coupling. In Proceedings of the SPE Reservoir Simulation Symposium, Houston, TX, USA, 14–17 February 1999. [[CrossRef](#)]
42. Ito, Y.; Settari, A.; Kry, P.; Jha, K. Development and Application of Pseudo-Functions for Reservoir Simulation to Represent Shear Failure During the Cyclic Steam Process. In Proceedings of the SPE International Thermal Operations Symposium, Bakersfield, CA, USA, 8–10 February 1993. [[CrossRef](#)]
43. Gutierrez, M. Fully Coupled Analysis of Reservoir Compaction and Subsidence. In Proceedings of the European Petroleum Conference, London, UK, 25–27 October 1994. [[CrossRef](#)]
44. Du, J.; Wong, R. Development of a Coupled Geomechanics-Thermal Reservoir Simulator Using Finite Element Method. In Proceedings of the Canadian International Petroleum Conference, Calgary, AB, Canada, 7–9 June 2005. [[CrossRef](#)]
45. Morkos, P.; Gildin, E. Development of Agile Framework for Model-Order Reduction of Large-Scale Geomechanical Models: A Novel Workflow for Coupled Simulations. In Proceedings of the SPE/AAPG/SEG Unconventional Resources Technology Conference, Virtual, 20–22 July 2020. [[CrossRef](#)]
46. An, C.; Fang, Y.; Liu, S.; Alfi, M.; Yan, B.; Wang, Y.; Killough, J. Impacts of Matrix Shrinkage and Stress Changes on Permeability and Gas Production of Organic-Rich Shale Reservoirs. In Proceedings of the SPE Reservoir Characterisation and Simulation Conference and Exhibition, Abu Dhabi, United Arab Emirates, 8–10 May 2017. [[CrossRef](#)]
47. Amirlatif, A.; Eckert, A.; Nygaard, R.; Bai, B. Estimation of Reservoir Uplift, Seismicity and Failure Likelihood during CO<sub>2</sub> Injection through Coupled Reservoir Simulation. In Proceedings of the Canadian Unconventional Resources Conference, Calgary, AB, Canada, 15–17 November 2011. [[CrossRef](#)]
48. Xu, T.; Lindsay, G. Unique Multidisciplinary Approach to Model and Optimize Pad Refracturing in the Haynesville Shale. In Proceedings of the SPE/AAPG/SEG Unconventional Resources Technology Conference, Austin, TX, USA, 24–26 July 2017. [[CrossRef](#)]
49. Han, H.; Higgins-Borchardt, S.M.; Mata, D.; Gonzales, V.M. In-Situ and Induced Stresses in the Development of Unconventional Resources. In Proceedings of the SPE/CSUR Unconventional Resources Conference—Canada, Calgary, AB, Canada, 30 September–2 October 2014. [[CrossRef](#)]
50. Pei, Y.; Yu, W.; Sepehrnoori, K. Investigation of Vertical Fracture Complexity Induced Stress Interference in Multilayer Shale Gas Reservoirs with Complex Natural Fractures. In Proceedings of the SPE Annual Technical Conference and Exhibition, Virtual, 26–29 October 2020. [[CrossRef](#)]
51. Lei, Z.; Yang, X.; Li, X.; Hu, D.; Wu, Y.; Peng, Y. Advanced Modeling of Horizontal Well Performance Under Different Re-fracturing Designs in Tight Oil Reservoir. In Proceedings of the SPE Europec Featured at 81st EAGE Conference and Exhibition, London, UK, 3–6 June 2019. [[CrossRef](#)]
52. French, S.; Puspitasari, R.; Isherwood, A.; Cox, P.; Marsden, R.; Mbang, M.N.E.; Tan, C.P.; John, Z. 4-D Geomechanics to Predict Compaction and Subsidence for Development of Unconsolidated Sandstone Reservoirs: Fortuna Project Case Study, Offshore Equatorial Guinea. In Proceedings of the SPE/IADC Drilling Conference and Exhibition, The Hague, The Netherlands, 14–16 March 2017. [[CrossRef](#)]
53. Shokri, A.R.; Chalaturnyk, R.J.; Nickel, E. Non-Isothermal Injectivity Considerations for Effective Geological Storage of CO<sub>2</sub> at the Aquistore Site, Saskatchewan, Canada. In Proceedings of the SPE Annual Technical Conference and Exhibition, Calgary, AB, Canada, 30 September–2 October 2019. [[CrossRef](#)]
54. Kim, G.W.; Kim, T.H.; Lee, K.S. Impact of Heterogeneous Hydro-Geomechanical Properties of Caprock on CO<sub>2</sub> Leakage by Tensile Fracture Reactivation During CCS. In Proceedings of the Abu Dhabi International Petroleum Exhibition & Conference, Abu Dhabi, United Arab Emirates, 7–10 November 2016. [[CrossRef](#)]

55. Restrepo, A.; Rendón, N.; Marin, R.; Lara, V.; Osorio, G.; Velásquez, J.; Lopez, C.; Ocampo, A. Geomechanics Coupled Simulation of Different Completion Schemes in a Stress Sensitive Reservoir. In Proceedings of the EAGE Annual Conference & Exhibition incorporating SPE Europe, London, UK, 10–13 June 2013. [\[CrossRef\]](#)
56. Onaisi, A.; Samier, P.; Koutsabeloulis, N.; Longuemare, P. Management of Stress Sensitive Reservoirs Using Two Coupled Stress-Reservoir Simulation Tools: ECL2VIS and ATH2VIS. In Proceedings of the Abu Dhabi International Petroleum Exhibition and Conference, Abu Dhabi, United Arab Emirates, 13–16 October 2002. [\[CrossRef\]](#)
57. Bourgeois, F.; Koutsabeloulis, N. Geomechanical Modeling of a Full Reservoir of the North Sea. In Proceedings of the SPE/EAGE Reservoir Characterization and Simulation Conference, Abu Dhabi, United Arab Emirates, 28–31 October 2007. [\[CrossRef\]](#)
58. Wagner, R. *Stratygrafia Osadów i Rozwój Basenu Cechsztyńskiego na Niżu Polskim. Prace Państwowego Instytutu Geologicznego*, 146; Państwowy Inst. Geologiczny: Warszawa, Poland, 1994; OL924861M, LCCN: 95223745.
59. Kotarba, M.; Wagner, R. Generation potential of the Zechstein Main Dolomite (Ca<sub>2</sub>) carbonates in the Gorzów Wielkopolski-Miedzychód-Lubiatów area: A geological and geochemical approach to microbial-algal source rock. *Przegląd Geol.* **2007**, *55*, 1025–1036.
60. Czeakański, E.; Kwolek, K.; Mikołajewski, Z. Hydrocarbon fields in the Zechstein Main Dolomite (Ca<sub>2</sub>) on the Gorzów Block (NW Poland). *Przegląd Geol.* **2010**, *58*, 695–703.
61. Protas, A.; Wojtkowiak, Z. The Gorzów Block. Geology of the Lower Zechstein. In *Guide to 71st Congress of the Polish Geological Society*; Państwowy Inst. Geologiczny: Warszawa, Poland, 2000; pp. 163–171.
62. Dadlez, R. *Budowa Geologiczna Niecki Szczecińskiej i Bloku Gorzowa*; Prace PIG, 96; Państwowy Inst. Geologiczny: Warszawa, Poland, 1979; ISBN 108322000200, LCCN: 81118351.
63. Peryt, T.; Dyjaczynski, K. An isolated carbonate bank in the Zechstein Main Dolomite basin, western Poland. *J. Pet. Geol.* **1991**, *14*, 445–458. [\[CrossRef\]](#)
64. Jaworowski, K.; Mikołajewski, Z. Oil- and gas-bearing sediments of the Main Dolomite (Ca<sub>2</sub>) in the Międzychód region: A depositional model and the problem of the boundary between the second and third depositional sequences in the Polish Zechstein Basin. *Przegląd Geol.* **2007**, *55*, 1017–1024.
65. Słowakiewicz, M.; Mikołajewski, Z. Sequence stratigraphy of the Upper Permian Zechstein Main Dolomite carbonates in Western Poland: A new approach. *J. Pet. Geol.* **2009**, *32*, 215–233. [\[CrossRef\]](#)
66. Słowakiewicz, M.; Mikołajewski, Z. Upper Permian Main Dolomite microbial carbonates as potential source rocks for hydrocarbons (W Poland). *Mar. Pet. Geol.* **2011**, *28*, 1572–1591. [\[CrossRef\]](#)
67. Wagner, R.; Dyjaczynski, K.; Papiernik, B.; Peryt, T.M.; Protas, A. Palaeogeographic map of the Main Dolomite (Ca<sub>2</sub>) in Poland. In *Balance and Hydrocarbon Potential of the Dolomite in the Main Perm Basin of Poland*; Kotarba, M.J., Ed.; Archiwum WGGiOOE AGH: Kraków, Poland, 2000.
68. Terzaghi, K. Stress Conditions for the Failure of Saturated Concrete and Rock. Reproduced in *From Theory to Practice in Soil Mechanics. Proc. Am. Soc. Test. Mater.* **1945**, *45*, 181–197.
69. Zoback, M.D. *Reservoir Geomechanics*; Cambridge University Press: Cambridge, UK, 2010; ISBN -978-0-521-77069-9.
70. Belyadi, H.; Fathi, E.; Belyadi, F. (Eds.) Chapter Thirteen: Rock Mechanical Properties and In Situ Stresses. In *Hydraulic Fracturing in Unconventional Reservoirs*; Gulf Professional Publishing: Oxford, UK, 2017; pp. 207–224, ISBN 9780128498712. [\[CrossRef\]](#)
71. Guo, B.; Liu, X.; Tan, X. (Eds.) *Petroleum Production Engineering*, 2nd ed.; Gulf Professional Publishing: Oxford, UK, 2017; pp. i–iii, ISBN 9780128093740. [\[CrossRef\]](#)
72. Bratton, T.; Cooper, I. Wellbore Measurements: Tools, Techniques, and Interpretation. In *Advanced Drilling and Well Technology*; Aadnoy, B., Cooper, I., Miska, S., Mitchell, R., Payne, M., Eds.; Society of Petroleum Engineers: Richardson, TX, USA, 2009; pp. 443–457, ISBN 978-1-55563-145-1.
73. Herwanger, J.; Koutsabeloulis, N. *Seismic Geomechanics: How to Build and Calibrate Geomechanical Models Using 3D and 4D Seismic Data*; EAGE Publications, 181; EAGE: Bunnik, The Netherlands, 2011; ISBN 9781680156973.
74. Słota-Valim, M.; Gołabek, A.; Szott, W.; Sowizdział, K. Analysis of Caprock Tightness for CO<sub>2</sub> Enhanced Oil Recovery and Sequestration: Case Study of a Depleted Oil and Gas Reservoir in Dolomite, Poland. *Energies* **2021**, *14*, 3065. [\[CrossRef\]](#)
75. Kahraman, S.; Fener, M.; Kozman, E. Predicting the compressive and tensile strength of rocks from indentation hardness index. *J. South. Afr. Inst. Min. Metall.* **2012**, *112*, 331–339.
76. Sheorey, P.R. *Empirical Rock Failure Criteria*; A.A. Balkema: Rotterdam Brookfield, VT, USA, 1997; ISBN 9054106700.
77. Hoek, E. Rock Mechanics—An Introduction for the Practical Engineer Parts I, II, and III. *Min. Mag.* **1966**, *144*, 236–243.
78. Karaman, K.; Cihangir, F.; Ercikdi, B.; Kesimal, A.; Demirel, S. Utilization of the Brazilian test for estimating the uniaxial compressive strength and shear strength parameters. *J. South. Afr. Inst. Min. Met.* **2015**, *115*, 185–192. [\[CrossRef\]](#)
79. Yetkin, M.E.; Simsir, F.; Ozfirat, M.K.; Ozfirat, P.M.; Yenice, H. A Fuzzy Approach to selecting roof support in longwall mining. *S. Afr. J. Ind. Eng.* **2016**, *27*, 162–177. [\[CrossRef\]](#)
80. Tajduś, A.; Cała, M. Regarding the possibility of vertical delamination of the rocks overlying the mining excavations in LGOM. In Proceedings of the XXV Winter School of Rock Mechanics and Geoen지니어ing, Zakopane, Poland, 18–20 March 2022; KGBiG AGH: Kraków, Poland, 2002; pp. 701–712.
81. Adach-Pawelus, K.; Butra, J.; Pawelus, D. Assessment of the mining excavations stability using numerical methods. In *Aktualia i Perspektywy Górnictwa*; Wydział Geoinżynierii, Górnictwa i Geologii Politechniki Wrocławskiej: Wrocław, Poland, 2018; ISBN 978-83-946706-8-9.

82. Kolano, M.; Flisiak, D. Comparison of geomechanical properties of white rock salt and pink rock salt in Kłodawa salt diapir. *Stud. Geotech. Et Mech.* **2013**, *35*, 119–127. [[CrossRef](#)]
83. Jiang, D.; Lin, S.; Williams, P. Deformation path in high-strain zones, with reference to slip partitioning in transpressional plate-boundary regions. *J. Struct. Geol.* **2001**, *23*, 991–1005. [[CrossRef](#)]
84. Jarosiński, M. Recent tectonic stress regime in Poland based on analyses of hydraulic fracturing of borehole walls. *Przegląd Geol.* **2005**, *53*, 863–872.
85. Leverett, M. Capillary Behavior in Porous Solids. *Trans. AIME* **1941**, *142*, 152–169. [[CrossRef](#)]
86. Brooks, R.H.; Corey, A.T. Hydraulic Properties of Porous Media and Their Relation to Drainage Design. *Trans. ASAE* **1964**, *7*, 0026–0028. [[CrossRef](#)]
87. Szott, W.; Pańko, A.; Łętkowski, P.; Malaga, M. *Wykonanie Modeli Symulacyjnych dla złóż Ropy Naftowej Grotów–Międzychód–Lubiaków–Sowia Góra (Simulation Models of Grotów–Międzychód–Lubiaków–Sowia Góra Oil Field)*; INiG, Krosno; Dokumentacja wykonana dla PGNiG S.A.: Warszawa, Poland, 2007.
88. Rutqvist, J.; Wu, Y.-S.; Tsang, C.-F.; Bodvarsson, G. A modeling approach for analysis of coupled multiphase fluid flow, heat transfer, and deformation in fractured porous rock. *Int. J. Rock Mech. Min. Sci.* **2002**, *39*, 429–442. [[CrossRef](#)]
89. Settari, A.; Walters, D.A. Advances in Coupled Geomechanical and Reservoir Modeling with Applications to Reservoir Compaction. In Proceedings of the SPE Reservoir Simulation Symposium, Houston, TX, USA, 14–17 February 1999. [[CrossRef](#)]
90. Thomas, L.K.; Katz, D.L.; Tek, M.R. Threshold Pressure Phenomena in Porous Media. *Soc. Pet. Eng. J.* **1968**, *8*, 174–184. [[CrossRef](#)]
91. Vidal-Gilbert, S.; Nauroy, J.-F.; Brosse, E. 3D geomechanical modelling for CO<sub>2</sub> geologic storage in the Dogger carbonates of the Paris Basin. *Int. J. Greenh. Gas Control.* **2009**, *3*, 288–299. [[CrossRef](#)]
92. Lewis, R.W.; Sukirman, Y. Finite element modelling of three-phase flow in deforming saturated oil reservoirs. *Int. J. Numer. Anal. Methods Géoméché.* **1993**, *17*, 577–598. [[CrossRef](#)]
93. Tortike, W.; Ali, S.F. Reservoir Simulation Integrated with Geomechanics. *J. Can. Pet. Technol.* **1993**, *32*. [[CrossRef](#)]
94. Xikui, L.; Zienkiewicz, O. Multiphase flow in deforming porous media and finite element solutions. *Comput. Struct.* **1992**, *45*, 211–227. [[CrossRef](#)]
95. Inoue, N.; Fontoura, S.A.B. Explicit coupling between flow and geomechanical simulators. In Proceedings of the International Conference on Computational Methods for Coupled Problems in Science and Engineering, Ischia Island, Italy, 8–10 June 2009.
96. Tsang, C.-F. Linking thermal, hydrological, and mechanical processes in fractured rocks. *Annu. Rev. Earth Planet. Sci.* **1999**, *27*, 359–384. [[CrossRef](#)]
97. Słota-Valim, K.; Szott, W.; Łętkowski, P.; Rucinski, P.; Milek, K. A coupled flow—Geomechanics study on the effectiveness of methane drainage in multi-seam coal mine with the use of long-reach directional drilling. In Proceedings of the 2022 International Pittsburgh Coal Conference, Virtual, 19–22 September 2022.
98. Bear, J. *Dynamics of Fluids in Porous Media*; American Elsevier Publishing Company: New York, NY, USA, 1972; 764p, ISBN 9780444001146.
99. Min, K.-B.; Rutqvist, J.; Tsang, C.-F.; Jing, L. Stress-dependent permeability of fractured rock masses: A numerical study. *Int. J. Rock Mech. Min. Sci.* **2004**, *41*, 1191–1210. [[CrossRef](#)]
100. Min, K.-B.; Jing, L. Numerical determination of the equivalent elastic compliance tensor for fractured rock masses using the distinct element method. *Int. J. Rock Mech. Min. Sci.* **2003**, *40*, 795–816. [[CrossRef](#)]
101. Min, K.-B.; Rutqvist, J.; Tsang, C.-F.; Jing, L. Thermally induced mechanical and permeability changes around a nuclear waste repository—A far-field study based on equivalent properties determined by a discrete approach. *Int. J. Rock Mech. Min. Sci.* **2005**, *42*, 765–780. [[CrossRef](#)]
102. Ferrill, D.A.; Winterle, J.; Wittmeyer, G.; Sims, D.; Colton, S.; Armstrong, A.; Morris, A.P. Stressed Rock Strains Groundwater at Yucca Mountain, Nevada. *GSA Today—A Publ. Geol. Soc. Am.* **1999**, *5*, 1–8.
103. Byerlee, J. Friction of rocks. *Pure Appl. Geophys.* **1978**, *116*, 615–626. [[CrossRef](#)]
104. Ferrill, D.A.; Smart, K.J.; Morris, A.P. Resolved stress analysis, failure mode, and fault-controlled fluid conduits. *Solid Earth* **2020**, *11*, 899–908. [[CrossRef](#)]
105. Hangx, S.; Spiers, C.; Peach, C. The mechanical behavior of anhydrite and the effect of deformation on permeability development—Implications for caprock integrity during geological storage of CO<sub>2</sub>. *Energy Procedia* **2011**, *4*, 5358–5363. [[CrossRef](#)]
106. Labuz, J.F.; Zang, A. Mohr–Coulomb Failure Criterion. *Rock Mech. Rock Eng.* **2012**, *45*, 975–979. [[CrossRef](#)]
107. Zhang, Y.; Langhi, L.; Schaub, P.; Piane, C.D.; Dewhurst, D.; Stalker, L.; Michael, K. Geomechanical stability of CO<sub>2</sub> containment at the South West Hub Western Australia: A coupled geomechanical–fluid flow modelling approach. *Int. J. Greenh. Gas Control.* **2015**, *37*, 12–23. [[CrossRef](#)]
108. Pan, P.; Wu, Z.; Feng, X.; Yan, F. Geomechanical modeling of CO<sub>2</sub> geological storage: A review. *J. Rock Mech. Geotech. Eng.* **2016**, *8*, 936–947. [[CrossRef](#)]
109. Hoek, E.; Bieniawski, Z.T. Brittle fracture propagation in rock under compression. *Int. J. Fract.* **1965**, *1*, 137–155. [[CrossRef](#)]

**Disclaimer/Publisher’s Note:** The statements, opinions and data contained in all publications are solely those of the individual author(s) and contributor(s) and not of MDPI and/or the editor(s). MDPI and/or the editor(s) disclaim responsibility for any injury to people or property resulting from any ideas, methods, instructions or products referred to in the content.